

Addressing the Impact of Solar Modulation Systematic Uncertainties on Cosmic-Ray Propagation Models

Isabelle John,^{1,2,*} Alessandro Cuoco,^{1,2,†} and Mattia di Mauro^{2,‡}

¹*Dipartimento di Fisica, Università degli Studi di Torino,
via P. Giuria, 1 10125 Torino, Italy*

²*INFN – Istituto Nazionale di Fisica Nucleare, Sezione di Torino,
via P. Giuria 1, 10125 Torino, Italy*

We perform a comprehensive analysis of cosmic-ray propagation using the time-dependent AMS-02 flux measurements covering a full solar cycle, with particular emphasis on the role of solar modulation. We fit two representative Galactic propagation scenarios, convection- and re-acceleration-dominated models, in combination with three solar modulation prescriptions: the standard force-field approximation, an extended force-field model with a rigidity break, and the heliospheric propagation code `HelMod`. The inclusion of time-resolved antiproton data provides a unique probe of charge-sign-dependent modulation effects and low-energy systematics. We find that the force-field approximation can describe positively charged nuclei reasonably well outside the solar maximum in convection-dominated models, but fails during periods of high solar activity and for antiprotons at all times. In re-acceleration scenarios, strong degeneracies between solar modulation and low-energy propagation lead to unphysical results when simple modulation models are employed. Across all models, we identify systematic uncertainties of order 10–15% in the reconstructed local interstellar spectra and propagation parameters, driven by limitations in current solar modulation modelling. Compared to the percent level error of current measurements, these uncertainties significantly limit the precision of cosmic-ray studies. Future time-dependent measurements spanning a full 22-year solar cycle will be crucial to reduce these uncertainties.

I. INTRODUCTION

The Sun plays a crucial role in shaping the local cosmic-ray fluxes. Due to a combination of solar winds and the heliospheric magnetic field, the cosmic-ray fluxes below rigidities of $\mathcal{O}(30-40)$ GV are strongly suppressed, a process referred to as solar modulation [1–5]. The exact mechanisms are complex and still subject to sizeable uncertainties, which, in turn, introduces systematic uncertainties in cosmic-ray propagation models [6–15].

However, detailed and dependable knowledge of the cosmic-ray fluxes is crucial to understand the origin of cosmic rays and the processes that take place during their acceleration and propagation throughout the Galaxy and within the solar system. Additionally, precise and reliable cosmic-ray models are necessary in the search for unexpected or exotic components in the cosmic-ray fluxes, for example from dark matter [16–19].

The effects of solar modulation were spectacularly confirmed in 2012 and 2018, when the Voyager I and Voyager II space probes, respectively, left the heliosphere and entered interstellar space. As expected, the cosmic-ray fluxes increased at lower energies [8, 20]. To this date, the Voyager probes provide the only measurements of the unmodulated cosmic-ray fluxes, *i.e.* the local interstellar spectra (LIS), offering valuable insights into the Sun's

impact on cosmic-ray propagation.

Moreover, the Sun's activity changes over an 11-year cycle, which adds a temporal dependence to the modulation of the cosmic-ray fluxes [1, 2]. During solar maximum, solar activity is strongest, and the heliospheric magnetic field is the most turbulent, as it is in the process of reversing its polarity. During solar minimum, the Sun is in a calmer state and its magnetic field more regular. This time-variation in solar activity is imprinted on the cosmic-ray fluxes by suppressing them more during periods of higher solar activity and less during periods of lower activity. This is illustrated in Figure 1: The top panel shows the number of sunspots, averaged over each month from the beginning of 2008 to the end of 2025 [21], *i.e.* from the beginning of solar cycle 24 until the most recent data of solar cycle 25. The number of sunspots strongly correlates with solar activity, and therefore anti-correlates with the modulation of the cosmic-ray fluxes, shown in the bottom panel for protons (orange circle markers) and antiprotons (burgundy diamond markers) as measured by AMS-02 [22, 23], spanning nearly a full solar cycle. Fluxes are shown at each Bartels rotation (*i.e.* the 27-day period that it takes until the same location on the Sun's equator is again visible from Earth), and are integrated over the rigidity range from 5 to 41 GV. Temporal changes in the intensity of the fluxes of $\sim 20\%$ are observed. The fluxes are most suppressed in 2014, which corresponds to the maximum of solar cycle 24 (spanning from 2008 to 2019). Currently, the Sun is undergoing solar cycle 25, which started in 2020 and is expected to peak around 2024–2025. The anti-correlation between solar activity and cosmic-ray fluxes was also shown by PAMELA, through the mea-

* E-mail: isabelle.john@unito.it, ORCID: [0000-0003-2550-7038](https://orcid.org/0000-0003-2550-7038)

† E-mail: alessandro.cuoco@unito.it, ORCID: [0000-0003-1504-894X](https://orcid.org/0000-0003-1504-894X)

‡ E-mail: mattia.dimauro@to.infn.it, ORCID: [0000-0003-2759-5625](https://orcid.org/0000-0003-2759-5625)

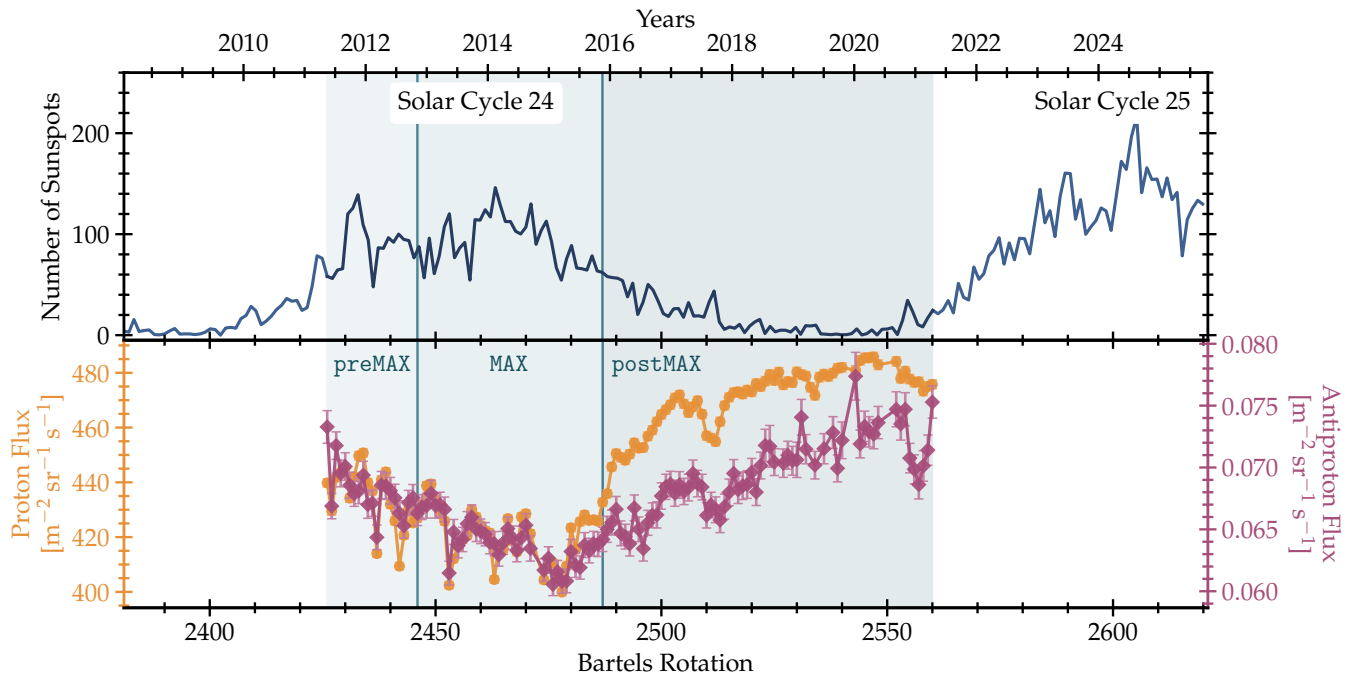


FIG. 1: The monthly-averaged number of sunspots [21] (top panel) and the cosmic-ray proton (orange circle markers) and antiproton (burgundy diamond markers) fluxes as measured by AMS-02 [22, 23] (bottom panel). The cosmic-ray fluxes are shown for rigidities between 5 GV and 42 GV for each Bartels rotation from May 2011 to January 2021. The **preMAX**, **MAX** and **postMAX** periods indicate the separate fitting periods in our analysis. A larger number of sunspots indicates stronger solar activity, which is anti-correlated with the intensity of the cosmic-ray fluxes. Due to the time-lag of the propagation of the solar winds and magnetic field, the imprint of solar activity on the cosmic-ray fluxes is typically delayed by a few months to a year.

surement of time-dependent proton [24], electron [25] and positron fluxes [26] across solar cycles 23 and 24.

Temporal changes correlating with the modulation of the cosmic-ray fluxes have also been detected in the solar γ -ray emission of the solar disk and halo, associated with interactions of cosmic rays with both photospheric gas and sunlight [27–30], further highlighting the extensive impact of solar activity on the solar system.

Cosmic-ray solar modulation can be modelled in terms of propagation in the heliosphere through the Parker equation, which includes convection, diffusion, drifts, and adiabatic energy losses [3–5]. To this purpose, various codes have been developed, such as **Helioprop** [31], **SolarProp** [32] and **HelMod** [33], of which the latter is the most advanced. Nonetheless, even within the framework of Parker propagation, numerous assumptions and ingredients (for example on the geometry of the diffusion tensor or on the overall level of diffusion) are required to derive the modulated flux of cosmic rays at Earth, which are subject to further uncertainties [33]. For this reason, many approximate-phenomenological models have been developed, which are easier to handle at the price of neglecting some of the complexity of the true process. Among these, the most commonly employed is the force-field approximation [34–36] which compresses the whole solar modulation process into a single parameter, *i.e.*, the force-field potential. A number of extended and modified versions of the force-field potential also exists, which im-

prove the modelling of the time-, charge-, and rigidity dependence of solar modulation (*e.g.* [9, 13, 37–43]). In the following we will use both force-field and extended force-field modulation models, as well as **HelMod** modulation in order to explore the systematic uncertainties related to solar modulation, and quantify their effect on the reconstruction of the cosmic-ray LIS and propagation in the Galaxy.

Recently, the AMS-02 experiment has released data of the fluxes of many cosmic-ray nuclei over a full solar cycle [22, 23], ranging from May 2011 until June 2022. Importantly, AMS-02 has also measured the fluxes of antiprotons, which, as negatively charged cosmic rays, are impacted differently compared to protons and other positively charged nuclei, due to charge-sign effects involved in solar modulation. This can be seen in the bottom panel of Fig. 1, where, indeed, the time behaviour of the proton and antiproton fluxes are very different. The high-statistical precision of the AMS-02 data over a full solar cycle allows for a detailed study of the impact of solar activity on the locally measured cosmic rays. Studying the temporal effects makes it possible to investigate solar modulation during different configurations of solar activity, which can be governed by a variety of uncertainties, and in turn results in different modelling requirements.

In this work, we utilise the time-dependent AMS-02 data to investigate solar modulation, and the underlying systematic uncertainties that affect our ability to

precisely model cosmic-ray propagation. In particular, we conduct detailed parameter fits of cosmic-ray Galactic propagation models during three periods of different levels of solar activity, highlighted in Fig. 1. We combine this with various solar modulation models to gain an understanding of their impact on cosmic-ray propagation models and their systematic limitations. Ideally, if both the Galactic propagation and solar modulation models are correct, the results should be independent of the analysed time-period. We will thus investigate the consistency of the LIS fluxes and of the solar modulation potentials derived in the three differing periods to examine if a coherent picture emerges.

The remainder of this article is structured as follows: In Section II, we list the cosmic-ray datasets used throughout our analysis. In Section III, we describe our cosmic-ray propagation models, and in Section IV the solar modulation models investigated in our analysis. We present and discuss our results in Section V, and provide conclusions in Section VI.

II. COSMIC-RAY DATA SELECTION

AMS-02 has recently released time-dependent data for many cosmic-ray species with high statistical precision. These datasets span a time period corresponding to a full solar cycle¹, from May 2011 to November 2022 (mostly solar cycle 24), allowing us to track changes in the local cosmic-ray flux over a full cycle of solar activity. To study these effects, we conduct both time-dependent and time-integrated fits to the data.

As reference, we perform fits using the *7-year time-integrated* AMS-02 dataset [44]. This dataset spans from May 2011 to May 2018 and includes protons, Helium, Carbon, Oxygen, and Nitrogen, as well as the antiproton-to-proton ratio, Boron-to-Carbon ratio and Helium-3-to-Helium-4 ratio. We also include the proton data from CALET [45] up to ~ 10 TeV/nuc, the Helium data from DAMPE [46] up to ~ 10 TeV/nuc, and the Boron-to-Carbon ratio from DAMPE [47]. Furthermore, we use the data from the Voyager probes, as they provide measurements of the unmodulated LIS fluxes for protons and Helium outside the heliosphere at rigidities below ~ 1 GV [20].

We then perform further fits using the recently published *time-dependent* AMS-02 datasets. Specifically, we include the time-dependent data for antiprotons and protons [22], and for the cosmic-ray nuclei Helium, Boron, Carbon, Nitrogen, and Oxygen [23], as well as the Boron-to-Helium ratio [23] (as, unfortunately, the

time-dependent Boron-to-Carbon ratio has not been provided by AMS-02), and the time-dependent Helium-3-to-Helium-4 ratio [48]. Due to large uncertainties in their production cross sections, we do not fit to data for Lithium and Beryllium [49]. The above time-dependent datasets, however, only reach up to ~ 41 GV for antiprotons and protons, and ~ 60 GV for the other nuclei. Above these rigidities, where solar modulation is subdominant, we thus complement the data with the 7-year time-integrated AMS-02 dataset [44].

Furthermore, for consistency, we only include data above a rigidity of 2 GV, as data below this rigidity is only given for protons and antiprotons, but not the other nuclei. This does not apply to the Voyager data, which we fit directly to the LIS fluxes below 1 GV.

Since the Helium-3-to-Helium-4 time-dependent AMS-02 data is only provided until April 2021, we restrict our time range from May 2011 until April 2021 for all datasets, even if time-dependent data for other nuclei is given over the full solar cycle.

To study the different phases of solar activity over a solar cycle, we divide this data into three time-integrated periods (see Fig. 1). These correspond to

- **preMAX**: May 2011 to November 2012 (Bartels rotations 2426 to 2446), *i.e.* a few months before the maximum of the solar activity,
- **MAX**: December 2012 to November 2015 (Bartels rotations 2447 to 2487), *i.e.* the period where solar activity is maximal, and
- **postMAX**: December 2015 to April 2021 (Bartels rotations 2488 to 2560), *i.e.* the time after the maximum, where the polarity of the solar magnetic field is flipped compared to **preMAX**. This period also includes the solar minimum in around 2020.

Since the time-dependent data is given for each Bartels rotation (or every four Bartels rotation, in the case of the Helium-3-to-Helium-4 ratio), we create each time-integrated dataset by time-averaging the fluxes in each time period. We add statistical uncertainties in quadrature, divided by the square root of their total number. The combined systematic uncertainty is, instead, derived as a time-average of the individual uncertainties of each datapoint. We then compute the total uncertainty by adding statistical and systematic uncertainties in quadrature. We note that our treatment of the systematic uncertainties is somewhat approximate, as we do not have detailed information on the origin and interplay of the underlying systematics. For the future, besides the monthly datasets, we advocate the release of yearly or bi-yearly aggregated datasets from the AMS-02 collaboration in order to perform this kind of time-dependent analyses more easily. In principle, one could perform analyses using the monthly datasets directly. However, this is not optimal since it requires the use of many fit parameters (*i.e.*, an independent solar modulation potential in each

¹ Note the liberal use of the term “solar cycle”. While a solar cycle is defined from solar minimum to solar minimum, we also adopt the term to represent any ~ 11 -year period of solar activity, such as the period covered by the time-dependent AMS-02 data.

Bartels rotation), or a model of the time-dependent modulation (as *e.g.* in [9, 10, 37, 38, 42, 43]), which, however, introduces further model dependency.

Fig. 1 illustrates our choice of these periods. The number of sunspots strongly anti-correlates with the cosmic-ray fluxes, clearly indicating periods of lower solar activity before and after the maximum phase. However, the imprint of solar activity on the cosmic-ray fluxes is subject to a time-lag due to the propagation time of the heliospheric magnetic field and solar winds. This lag is estimated to be around 2 to 14 months, and strongly depends on the rigidity of the cosmic rays, such that the lag time decreases with increasing rigidity [50, 51]. It can also be observed that the time lag is stronger during higher solar activity, by comparing the peak of the sunspot number in around 2014 to the dip in the cosmic-ray fluxes in around 2015, spanning almost a year. Conversely, during low solar activity, the lag is much shorter, as can be seen in the small peak in late 2020 that corresponds to a dip in the cosmic-ray fluxes occurring only a few months afterward. These observations allow us to estimate the period where the cosmic-ray fluxes are maximally modulated to be around December 2012 to November 2015 (MAX). The **preMAX** phase includes all data available before this, and the **postMAX** phase all data after this. However, since the available data before the MAX phase only encompass about 1.5 years, which is several years after the previous solar minimum, the **preMAX** phase somewhat resembles the MAX phase, and, as can be observed in Fig. 1, also includes periods of higher solar activity, like the spike in late 2011. The 7-yr dataset, instead, spanning from May 2011 to May 2018 encompasses all the **preMAX** and MAX periods and the beginning of the **postMAX** phase, *i.e.* it mostly includes the phase of high solar activity.

III. COSMIC-RAY PROPAGATION MODELS

Our analysis is based on the framework for cosmic-ray propagation models developed in previous works [52–56]. We use the numerical cosmic-ray propagation code GALPROP [57, 58] that takes into account a variety of processes such as cosmic-ray injection, diffusion, convection, energy losses and re-acceleration. In order to fit over the complex multi-dimensional parameter space, we use MultiNest [59]. Our free parameters include various parameters for cosmic-ray injection and propagation in the Galaxy. Very importantly, we also include parameters that take into account and parametrize the uncertainties in the production cross-sections of secondary cosmic rays [49, 60–64]. Depending on the solar modulation model (discussed in detail in Section IV), a number of additional free parameters is introduced. Within our framework, we fit solar-modulation and cosmic-ray parameters simultaneously, which accounts for the possible presence of degeneracies and interplay among all the parameters. For a full list of the fit parameters, see the figures and tables in Appendix C, and the references above for more

details.

We use two benchmark propagation models that differ in a few free parameters, focusing on cosmic-ray convection (**conv**) and re-acceleration (**reacc**), respectively:

- **conv**: The *convection* propagation model includes the convection velocity through the parameter $v_{0,c}$, which describes the bulk motion of cosmic rays due to Galactic winds, perpendicular to the Galactic plane. In this model, re-acceleration is absent, and primary species have a single power-law injection spectrum without any breaks. The slope of the spectrum is $\gamma_{1,p}$ for protons, $\gamma_{1,He}$ for Helium and $\gamma_{1,CNO}$ for all other primary nuclei. This model also features a break in the diffusion spectrum, $R_{D,1}$, with a prior of $(2-6) \times 10^3$ MV and a corresponding smoothing factor of the spectrum, $s_{D,1}$. Note that also a second diffusion break is included at higher rigidities of about 200×10^3 GV, with $R_{D,2}$ and $s_{D,2}$, as a standard free parameter for both our propagation models.
- **reacc**: In the *re-acceleration* propagation model, the Alfvén velocity, v_A , that determines the magnitude of re-acceleration of low-energetic cosmic rays, is a free parameter with prior $0-35$ km/s. Convection is not included. Furthermore, the additional low-energy break in the diffusion spectrum is not present. Instead, we introduce a break in the injection spectrum, R_{inj} , with prior $(3-15) \times 10^3$ MV, and a corresponding smoothing factor, s_{inj} . The break is the same for all the species, while three more parameters corresponding to the three injection slopes below the break are introduced, $\gamma_{0,p}$ for protons, $\gamma_{0,He}$ for Helium and $\gamma_{0,CNO}$ for the other primary nuclei.

Our choice to distinguish between models with and without re-acceleration is due to the uncertainties related to this process. The role of re-acceleration has been debated in the recent literature, and it is unclear to what extent it contributes to (re-)accelerating cosmic rays at energies of a few to tens of GeV [65].

IV. SOLAR MODULATION OF GALACTIC COSMIC RAYS

A. General Framework

Galactic cosmic-rays entering the heliosphere experience significant, time-dependent modifications to their spectra (and, to a lesser extent, composition) at kinetic energies below $\mathcal{O}(30-40)$ GeV. These effects arise from transport through the expanding solar wind and the large-scale heliospheric magnetic field (HMF), superimposed with a turbulent magnetic component that governs particle scattering. Solar modulation is therefore controlled by solar-cycle conditions and depends on rigidity

$R \equiv pc/|q|$ (rather than energy alone), particle speed β , and, crucially, the sign of the electric charge [1, 3–5]. As a result, cosmic-ray spectra measured near Earth differ from the LIS fluxes, and an explicit heliospheric transport model is required whenever low-energy data are used for precision physics, including antimatter studies and dark-matter searches.

The standard description is provided by the Parker transport equation, a Fokker–Planck equation for the phase-space density $f(\vec{r}, p, t)$ [3, 4]:

$$\frac{\partial f}{\partial t} = -(\vec{V}_{\text{sw}} + \vec{v}_d) \cdot \nabla f + \nabla \cdot (\mathbf{K} \cdot \nabla f) + \frac{1}{3}(\nabla \cdot \vec{V}_{\text{sw}}) p \frac{\partial f}{\partial p}. \quad (1)$$

Here, \vec{V}_{sw} is the solar-wind velocity (typically outward and approximately radial), \mathbf{K} is the diffusion tensor (encoding scattering on magnetic turbulence), and \vec{v}_d is the drift velocity associated with the antisymmetric part of \mathbf{K} , accounting for gradient/curvature drifts and current-sheet drifts. The last term describes adiabatic energy changes due to the diverging solar wind, which generally act as energy losses for cosmic-ray propagating inward. Although all terms are always present, their relative importance depends strongly on rigidity and on whether the heliosphere is in a solar-minimum or solar-maximum state [1, 5].

Diffusion: Spatial diffusion, described by the symmetric part of \mathbf{K} , is controlled by scattering on the turbulent HMF and is usually modelled with different parallel and perpendicular components with respect to the large-scale field. In practice, modulation at fixed rigidity increases when the diffusion normalization decreases (stronger scattering), or when the HMF magnitude and turbulence level increase. Modulation is, thus, stronger during solar maximum when the enhanced solar activity tends to increase magnetic irregularities, reducing the effective mean free path and thereby lowering the diffusion coefficient [1, 66]. Conversely, modulation is weaker during solar minimum when the field is more ordered and diffusion is more efficient. Independently of the solar cycle, diffusion effects rapidly weaken above $\sim 10 - 20$ GV, where heliospheric transport becomes subdominant and the observed spectra approach the LIS.

Convection and adiabatic energy losses: Convection by the solar wind and adiabatic losses are largely charge independent and together set a baseline modulation that is always present, most relevant at rigidities below a few GV [4, 34]. Increasing V_{sw} (or, more generally, the effective residence time in the expanding wind) enhances adiabatic losses and steepens the low-energy suppression. These terms are therefore particularly important when modelling the overall softening of low-rigidity spectra, even in periods when charge-sign effects are weak.

Drifts and charge-sign dependence: A distinctive feature of Eq. (1) is particle drift, which introduces a strong dependence on the sign of the charge q [67]. The drift pattern depends on the global HMF polarity, commonly denoted by A , which reverses approximately every 11 years.

In an $A > 0$ polarity epoch (defined as the HMF lines pointing outwards at the solar north pole, and inwards at the south pole), positively charged particles preferentially drift inward through the polar regions, where they can reach the inner heliosphere efficiently, resulting in a weak modulation. On the other hand, negatively charged particles enter more efficiently through the equatorial plane along the heliospheric current sheet (HCS), *i.e.*, the thin border between positive and negative polarity of the magnetic field. The HCS can be highly warped, and its geometry—often summarized by a tilt angle that increases from solar minimum to maximum—strongly inhibits propagation and increases energy losses for particles whose access to the inner heliosphere is governed by current-sheet trajectories [1, 66], reducing the flux of these particles near Earth. Conversely, the situation is flipped during negative polarity ($A < 0$); positively charged particles will be more modulated, and negatively charged particles less.

Solar minimum vs. maximum: The solar-cycle dependence can be summarized as follows: (i) during *solar minimum*, the HMF is more ordered and the HCS is less tilted, so drift effects are comparatively large and the modulation becomes more charge-sign dependent; at the same time, diffusion is more efficient, reducing the overall modulation strength at a given rigidity. (ii) during *solar maximum*, enhanced turbulence suppresses drifts and lowers the effective diffusion coefficient, leading to stronger overall modulation but a more charge-symmetric behavior [1]. Accordingly, the most pronounced particle/antiparticle differences are expected at low rigidities (typically $\lesssim 5 - 10$ GV) during solar minima, and especially when comparing data taken in opposite polarity epochs. These expectations are borne out by time-dependent measurements from PAMELA and AMS-02, which show both strong temporal evolution of the absolute fluxes and clear signatures of charge-sign dependent modulation in appropriate phases of the solar cycle [8, 24, 68].

Putting together the above consideration, this means that during our defined **preMAX** phase, when $A < 0$, protons are more modulated than antiprotons. In the **postMAX** phase, when $A > 0$ the opposite is true, and the antiproton flux is stronger suppressed than the proton flux. This can be seen in Fig. 1 where, lasting for about one year from 2015 to 2016, the proton flux raises much more quickly than the antiproton flux, highlighting the transition between the two regimes. The above considerations will thus guide our expectations for the level of modulation of protons and antiprotons derived from the results of the fits performed in the three periods.

B. Solar Modulation Models

Numerical solutions of Eq. (1) with realistic heliospheric inputs, including the HMF magnitude, HCS tilt evolution, and drift suppression by turbulence, are im-

plemented in dedicated frameworks [1, 31, 32, 69, 70]. However, these approaches are typically time-consuming and numerically expensive. For this reason, alternative simplified frameworks have been developed. The most commonly employed approach is the force-field approximation, which compresses the combined effects of diffusion, convection, and adiabatic losses into a single modulation potential, and can be derived further assuming steady-state homogeneous and spherically symmetric propagation [34]. This approach, thus, cannot describe charge-sign dependence and polarity effects. On the other hand, charge-sign effects can be re-introduced in an effective way using separate potentials for positively and negatively charged particles. Further extensions of the force-field approach consider a rigidity-dependent potential [9, 38, 41].

In the following, we will thus study the impact of solar modulation and the chosen solar-modulation models by carrying out our analysis for three different solar modulation models: (1) the simple and widely used force-field potential [34], (2) an extended force-field potential [41] that allows for a rigidity dependence of the solar modulation potential, and (3) by applying the `HelMod` model [33, 69, 70]. Below, we briefly describe each model.

The *force-field potential* relates the locally measured flux, Φ_{loc} , to the flux in the local interstellar medium (*i.e.*, the LIS), Φ_{LIS} , through [34]

$$\Phi_{\text{loc}}(E) = \Phi_{\text{LIS}}(E + \phi Z/A) \times \frac{E \times (E + 2m_p)}{(E + \phi Z/A) \times (E + \phi Z/A + 2m_p)}, \quad (2)$$

where E is the kinetic energy per nucleon, Z and A are the charge and mass number of the nuclei, m_p is the proton mass, and ϕ the solar modulation potential. In our fit, this corresponds to two free parameters, ϕ_p for positively charged cosmic rays, and $\phi_{\bar{p}}$ for negatively charged cosmic rays (*i.e.* antiprotons, as we do not fit to electron (or positron) data).

The *extended model* modifies the force-field potential ϕ in Eq. 2 by introducing a rigidity-dependence on the potential $\phi_{\text{Ext}}(R)$, defined by [41]

$$\phi_{\text{Ext}}(R) = \phi_l + \frac{\phi_h - \phi_l}{1 + \exp(-R + R_{br})}, \quad (3)$$

where ϕ_l and ϕ_h are the modulation potential at low and high rigidities, respectively, and R_{br} is a break in rigidity separating the two potentials. In our fits, this results in 5 free parameters: a low and high potential for positively and negatively charged cosmic rays denoted by $\phi_{l,p}$, $\phi_{h,p}$, $\phi_{l,\bar{p}}$ and $\phi_{h,\bar{p}}$, respectively, as well as the break R_{br} , which is applied to both negatively and positively charged cosmic rays simultaneously.

The *heliospheric modulation model*, `HelMod` [33, 69, 70], is a cosmic-ray propagation code based on the full solution of Eq. 1. While a full simulation is complex, the

`HelMod` team provides matrices that allow a simple calculation of solar modulation from a LIS, for specific fits to AMS-02 datasets. We make use of the `HelMod` matrices corresponding to our selected AMS-02 datasets in our analysis, but note that these matrices were developed for an assumed LIS [14, 15, 71]. This means that, since we fit our own propagation model, `HelMod` cannot provide fully self-consistent modulation in our analysis. Despite this, `HelMod` is the only solar modulation model, among the three we consider, that fully models cosmic-ray propagation in the heliosphere, and thus offers an important comparison to the other solar modulation models investigated in our analysis. Note that for the `HelMod` fits, there is no free parameter describing solar modulation.

We conduct time-integrated fits for the force-field, extended model and `HelMod`. We also perform time-dependent fits for the force-field and extended solar modulation model. Due to the limitations described above, however, we do not perform a time-dependent fit with `HelMod`. For these time-dependent fits, we separately and independently fit to each of the three time periods described in Section II, *i.e.* `preMAX`, `MAX` and `postMAX`, which allows us to investigate each modulation model for different configurations of solar activity. Furthermore, this enables us to study in detail the effects of the chosen solar modulation model on the propagation parameters.

V. RESULTS AND DISCUSSION

In the following, we mainly focus on the consequences of our results for solar modulation. The full results for each fit are reported in Appendix C, both in tabular form and in graphical form. We choose to focus on the results for protons and antiprotons, but provide further plots for the other cosmic-ray nuclei in Appendix A and B.

Figure 2 shows results for the three solar modulation models in the 7-yr time-integrated fits for the conv propagation model. The left panel shows the proton fluxes and the right panel the antiproton fluxes. Dashed lines represent LIS fluxes, while solid lines are fluxes that are modulated using the force-field potential (orange), the extended model (burgundy) and `HelMod` (green). The corresponding AMS-02 data is given in dark grey, where empty markers correspond to data points that are not included in the fit. The bottom of each plot shows the residuals between the data and the modulated fluxes. For protons, both the force-field and extended model fit the data very well to within $\sim 1\sigma$, only showing some worsening of the fit below ~ 3 GV, and provide very similar LISes. The `HelMod` case, instead, provides a significantly worse fit and a sizeable different LIS. For the antiproton fluxes, the results are more consistent between the three modulation models, both in the LIS fluxes, which are very similar, and the residuals. This is somewhat expected as cosmic-ray antiprotons are produced as secondaries in interactions of cosmic-ray protons with ener-

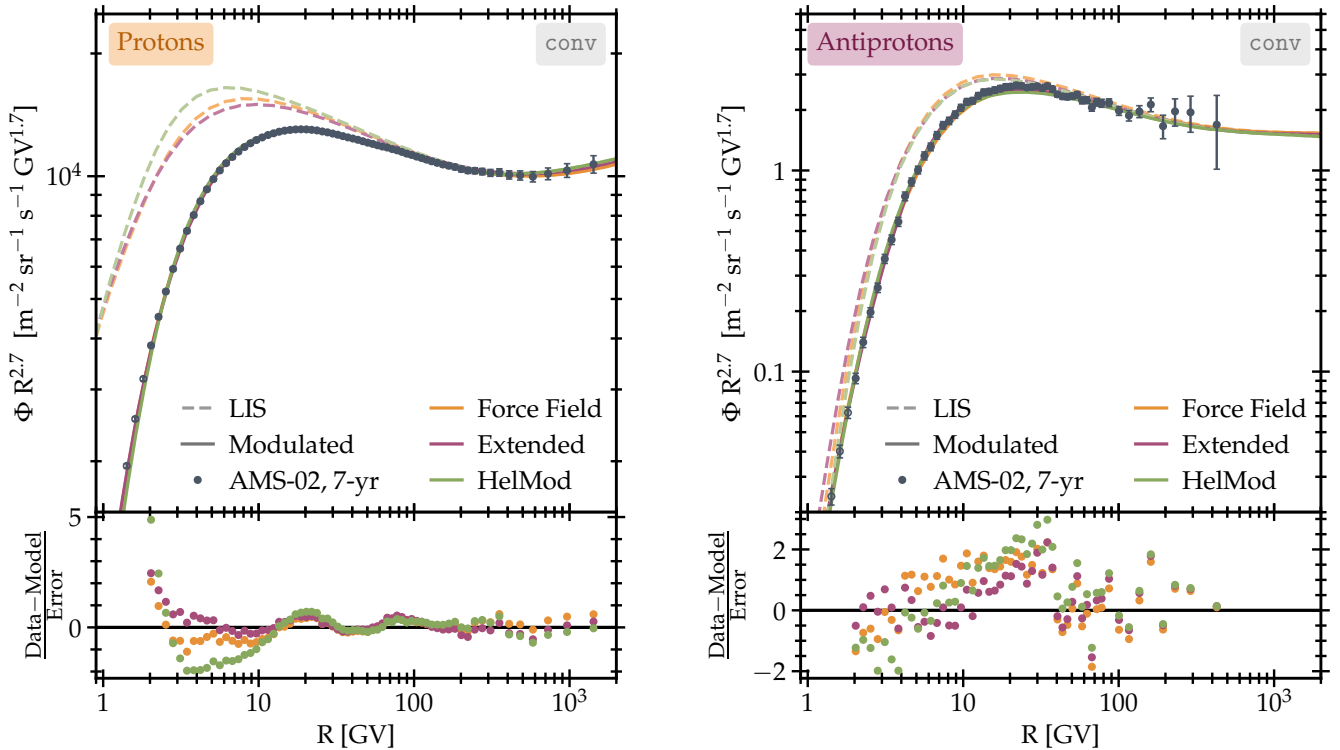


FIG. 2: The spectra for protons (left panel) and antiprotons (right panel) for the `conv` propagation model. In each plot, the LIS (dashed line) and modulated flux (solid) line are given for a different solar-modulation model: the force-field potential (orange), the extended force-field potential (burgundy) and the `HelMod` model (green). The residuals in each plot are compared to the 7-yr AMS-02 data.

gies of ~ 8 GeV or higher, where the proton LIS fluxes are only weakly affected by solar modulation. We also recover an antiproton excess at $\sim 20 - 30$ GV, as in previous studies [16, 17, 52, 72–75]. We do not attempt here to quantify the significance of this excess, a task that requires a specific analysis and is postponed to a dedicated study.

It follows from Fig. 2, that in principle, `HelMod` provides a detailed modelling of cosmic-ray propagation in the heliosphere and is able to capture many processes that are overlooked in the effective solar modulation models. However, in our scenario the `HelMod` fit shows the strongest discrepancy below about 10 GV in the proton fluxes, significantly worse than the force-field and extended model. We believe this is due to the fact that the `HelMod` modulation computation provided by the `HelMod` team is based on an underlying LIS that was optimised together with `Galprop` [33]. In particular, in [33] the injection spectra of the primary nuclei are parametrized differently than in our study and allow for a larger freedom. This highlights again that the proper implementation the `HelMod` model into our framework would require to re-derive simultaneously solar modulation and cosmic-ray propagation in a self-consistent way. This is, however, a non-trivial task which is left for future studies.

In Figure A.1 in Appendix A, we present the 7-yr fits also for the `reacc` propagation model, where we reach

similar conclusions.

Table I summarises the best-fit values of the solar modulation parameters from our analysis. As expected, across all time-dependent scenarios, solar modulation is strongest during the `MAX` period, and weakest during the `postMAX` phase, which includes the minimum of solar cycle 24 in 2020. The `preMAX` phase, only covering a couple of years before the maximum phase, shows intermediate modulation, accordingly.

Looking at the values of the potential for the `conv` case and extended solar modulation in Tab. I, it can be seen that during the `preMAX` and `postMAX` phases, the lower and higher potential for protons ($\phi_{l,p}$ and $\phi_{h,p}$) are very similar, while they are incompatible during the `MAX` period. In practice, this implies that the simple force-field is a good approximation during phases of lower solar activity, while the more complex extended modulation is required during the solar maximum phase. This picture, however, is not confirmed for antiprotons, where the lower potential, $\phi_{l,\bar{p}}$, is significantly stronger than the higher potential, $\phi_{h,\bar{p}}$, across all fits, with a rigidity break $R_{br} \sim 5$ GV, that remains relatively consistent throughout the three time periods.

We consider two possible explanations for this behaviour: (1) A first possibility is that the antiproton LIS is incorrect. This, indeed, can be due to an incorrect propagation model, or more likely to an incorrect mod-

		Force-Field Potential				Extended Model			
		preMAX	MAX	postMAX	7-yr t.-i.	preMAX	MAX	postMAX	7-yr t.-i.
conv	ϕ_p [GV]	$0.52^{+0.01}_{-0.01}$	$0.68^{+0.01}_{-0.02}$	$0.31^{+0.01}_{-0.01}$	$0.47^{+0.01}_{-0.01}$	–	–	–	–
	$\phi_{\bar{p}}$ [GV]	$0.59^{+0.03}_{-0.02}$	$0.75^{+0.03}_{-0.04}$	$0.54^{+0.03}_{-0.02}$	$0.77^{+0.03}_{-0.02}$	–	–	–	–
	$\phi_{l,p}$ [GV]	–	–	–	–	$0.52^{+0.01}_{-0.01}$	$0.67^{+0.01}_{-0.01}$	$0.31^{+0.01}_{-0.01}$	$0.47^{+0.01}_{-0.01}$
	$\phi_{h,p}$ [GV]	–	–	–	–	$0.50^{+0.03}_{-0.03}$	$0.60^{+0.03}_{-0.03}$	$0.28^{+0.03}_{-0.03}$	$0.41^{+0.03}_{-0.03}$
	$\phi_{l,\bar{p}}$ [GV]	–	–	–	–	$0.82^{+0.07}_{-0.07}$	$1.02^{+0.05}_{-0.09}$	$0.81^{+0.06}_{-0.07}$	$0.95^{+0.05}_{-0.01}$
	$\phi_{h,\bar{p}}$ [GV]	–	–	–	–	$0.34^{+0.04}_{-0.04}$	$0.47^{+0.03}_{-0.04}$	$0.27^{+0.04}_{-0.04}$	$0.54^{+0.03}_{-0.02}$
	R_{br} [GV]	–	–	–	–	$4.86^{+0.54}_{-0.51}$	$5.03^{+0.62}_{-0.43}$	$4.64^{+0.41}_{-0.38}$	$3.95^{+0.31}_{-0.32}$
reacc	ϕ_p [GV]	$0.65^{+0.01}_{-0.01}$	$0.81^{+0.01}_{-0.01}$	$0.40^{+0.01}_{-0.01}$	$0.65^{+0.01}_{-0.01}$	–	–	–	–
	$\phi_{\bar{p}}$ [GV]	$0.36^{+0.03}_{-0.03}$	$0.49^{+0.05}_{-0.04}$	$0.38^{+0.03}_{-0.03}$	$0.55^{+0.06}_{-0.04}$	–	–	–	–
	$\phi_{l,p}$ [GV]	–	–	–	–	$0.55^{+0.01}_{-0.02}$	$0.70^{+0.02}_{-0.02}$	$0.34^{+0.01}_{-0.01}$	$0.54^{+0.02}_{-0.02}$
	$\phi_{h,p}$ [GV]	–	–	–	–	$0.28^{+0.03}_{-0.04}$	$0.37^{+0.04}_{-0.03}$	$0.12^{+0.01}_{-0.02}$	$0.29^{+0.03}_{-0.04}$
	$\phi_{l,\bar{p}}$ [GV]	–	–	–	–	$1.11^{+0.07}_{-0.06}$	$1.45^{+0.05}_{-0.02}$	$1.12^{+0.07}_{-0.09}$	$1.00^{+0.00}_{-0.00}$
	$\phi_{h,\bar{p}}$ [GV]	–	–	–	–	$0.42^{+0.04}_{-0.05}$	$0.58^{+0.04}_{-0.05}$	$0.40^{+0.05}_{-0.04}$	$0.64^{+0.03}_{-0.04}$
	R_{br} [GV]	–	–	–	–	$3.27^{+0.13}_{-0.13}$	$2.96^{+0.13}_{-0.13}$	$3.13^{+0.15}_{-0.18}$	$3.37^{+0.12}_{-0.10}$

TABLE I: Best-fit solar-modulation parameters for the force-field potential (ϕ_p , $\phi_{\bar{p}}$) and the extended model ($\phi_{l,p}$, $\phi_{h,p}$, $\phi_{l,\bar{p}}$, $\phi_{h,\bar{p}}$, R_{br}) for the 3 time periods, as well as the time-independent fits of the 7-yr time-integrated (7-yr t.-i.) data. Upper rows represent the values for the **conv**, while lower rows for the **reacc** model. Note that there are no free solar-modulation parameters in the **HelMod** fits.

elling of the antiproton production cross-section, which is indeed still affected by sizeable uncertainties [49, 60–64]. (2) A second possibility, which we believe is more likely, is a failure of the force-field approximation. This could be related to the peculiar LIS of the antiprotons, which has a peaked shape at few GV, unlike other species which instead have a power-law-like spectrum. This is illustrated in Figure 3, which shows the proton and antiproton fluxes as measured by AMS-02 [22, 23]. This peculiar antiproton spectrum is due to the secondary nature of the species which is produced mainly via the reaction $p + H \rightarrow p + p + p + \bar{p}$, which, with a high threshold of about 8 GeV, can only produce small amounts of low-energy antiprotons. A possibility is thus that the force-field approximation does not work well when applied to this peaked spectrum. Indeed, this seems to be confirmed by various considerations: (1) the very close coincidence between the position of the modulation break R_{br} and the peak of the spectrum at about 5 GV, (2) the fact that the force field gives poor antiproton residuals below ~ 10 GV, while the extended modulation and the **HelMod** model improve the quality of the fit significantly (see Fig. 2), and (3) a model-independent analysis by the AMS-02 collaboration [22] that has found that below ~ 5 GV the modulation of antiprotons has different characteristics than protons, electrons and positrons. In particular, the amplitude of the modulation of the latter three grows at lower rigidities, while it becomes constant

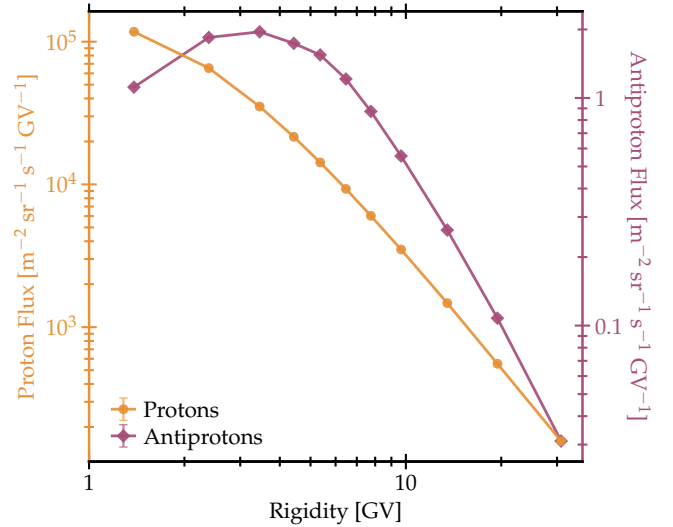


FIG. 3: The cosmic-ray proton (orange circle markers) and antiproton (burgundy diamond markers) fluxes from AMS-02 [22, 23]. The combined flux from Bartels rotation 2426 to 2560 is shown.

for antiprotons below ~ 5 GV. These hints, thus, seem to point toward a failure of the force-field potential to describe antiproton modulation well, although a definitive confirmation will require further studies.

The above picture is vastly different in the `reacc` propagation case. In the extended modulation model, as can be seen in Tab. I, the potentials above and below the break are very different both for protons and antiprotons during all three time periods. In principle, this implies that the force-field approximation is always inaccurate, even during phases of low solar activity, at least when re-acceleration is included in propagation models. We believe, however, that this is rather due to an unphysical result returned by the fit, as we describe in more detail further below.

Figure 4 shows the cosmic-ray proton and antiproton fluxes from our fits to the three time periods in the `conv` propagation model for the force-field and extended solar modulation. It can be noticed that the proton fit below 40 GV is significantly worse than what is achieved in the 7-yr dataset fit shown in Figure 2. This is mainly due to the fact that the time-dependent dataset for protons has only a few data points in rigidity, *i.e.*, only 11 between 1 and 41 GV, which is insufficient given the large statistics and percent rigidity resolution of AMS-02. This is opposed to the 7-yr dataset, which has 40 data points in the same rigidity range. This issue fortunately is not present for the other nuclei, which instead have an adequate number of data points. For the future, we advocate the release of homogenous time-dependent datasets for all the species from the AMS-02 collaboration.

Besides the above issue, the most important observation from Fig. 4 is that the proton LIS fluxes inferred in the three time periods show some discrepancy at a level of about 10%. This is contrary to expectations, where the LIS fluxes should be exactly the same, as we do not expect any temporal changes of the LIS fluxes on comparable time scales. This discrepancy is more severe for the pure force-field modulation, while the agreement improves for the extended modulation. Although 10% is not large in absolute terms, it is significantly larger than the percent-level statistical errors achieved by AMS-02. This discrepancy can be interpreted in two different ways: On one hand, this indicates that the current description of solar modulation is insufficient to self-consistently describe solar modulation effects over different phases of solar activity. In this respect, however, the extended models clearly provide a better modelling and should be preferred. On the other hand, this level of discrepancy can be understood as the current level of true, systematic uncertainty in the reconstructed LIS. Thus, the systematic uncertainties in propagation models are dominated by our limitation of solar modulation modelling. Finally, from Fig. 4 it can also be seen that the antiproton LIS fluxes are, instead, more stable and less affected by solar modulation systematic uncertainties, in agreement with the discussion for Fig. 2.

Figure 5 is similar to Fig. 4, but instead shows the LIS fluxes obtained from the time-dependent fits to the `reacc` propagation model. For protons in the force-field modulation case, the Fig. 5 confirms the same trend observed for the `conv` case, *i.e.*, a disagreement of the LIS fluxes

reconstructed in the three time periods, at the level of 10-15%. On the other hand, the LIS fluxes from the extended modulation model show a remarkable agreement. This, in principle, would indicate the ability of the extended modulation model to correctly describe solar modulation both in periods of high and low solar activity. However, the reconstructed LIS has a peculiar shape with a kink at around ~ 4 GV. Furthermore, this LIS also strongly differs from the LIS inferred through the force-field modulation. Additionally, the overall level of modulation is relatively low, even during the solar maximum, as can be seen from Tab. I. Overall, we believe this is an unphysical result likely due to the extra freedom present in the `reacc` model for the injection spectra, pointing towards difficulties in separating solar modulation effects from low-rigidity cosmic-ray transport effects, such as re-acceleration. This is illustrated in more detail at the end of this section.

We provide the LIS and modulated fluxes for the time-integrated fits over the 7-year dataset, as well as for the other cosmic-ray nuclei and ratios included in our fit in Appendix A.

Figures 6 and 7 show the temporal changes of the solar modulation potential throughout our fit period in the `conv` and `reacc` propagation model, respectively. For each of the three time periods, we use the best-fit LIS obtained from the fit for that time period, and compare to the proton and antiproton data to obtain the effective force-field solar modulation potential at each Bartels rotation. We do this both for the LISes obtained with the force-field (FF) and extended modulation (Ext) models. Furthermore, to determine the effective potential, we only include fluxes above rigidities of 5 GV, which lies above the break in the extended model throughout all propagation models (see Tab. I). This choice minimises the bias in the Ext model, as it now only includes a single potential (*i.e.*, above the break). Thus, this method offers a good illustration of the temporal changes in the intensity of solar modulation for both our models.

Generally, as discussed in Sec. IV, we expect that the modulation potential should be similar for protons and antiprotons during the period of the solar maximum, when solar activity is highest and the heliosphere most turbulent. Before the maximum of solar cycle 24, the heliospheric magnetic field polarity is such that protons experience stronger solar modulation effects, and after the maximum, when the magnetic field polarity has flipped, the antiproton flux should be stronger suppressed. This can be observed in the bottom part of Fig. 1. As the flux intensity is anti-correlated with the solar modulation potential, we expect the potential for protons to be slightly stronger than the potential for anti-protons in the `preMAX` phase, similar in the `MAX` phase, and weaker in the `postMAX` phase.

In Fig. 6, which shows the `conv` propagation model, we can see that the above expectations are roughly met, in particular in the force-field fit. In the extended modulation, the situation is somewhat borderline, as the pro-

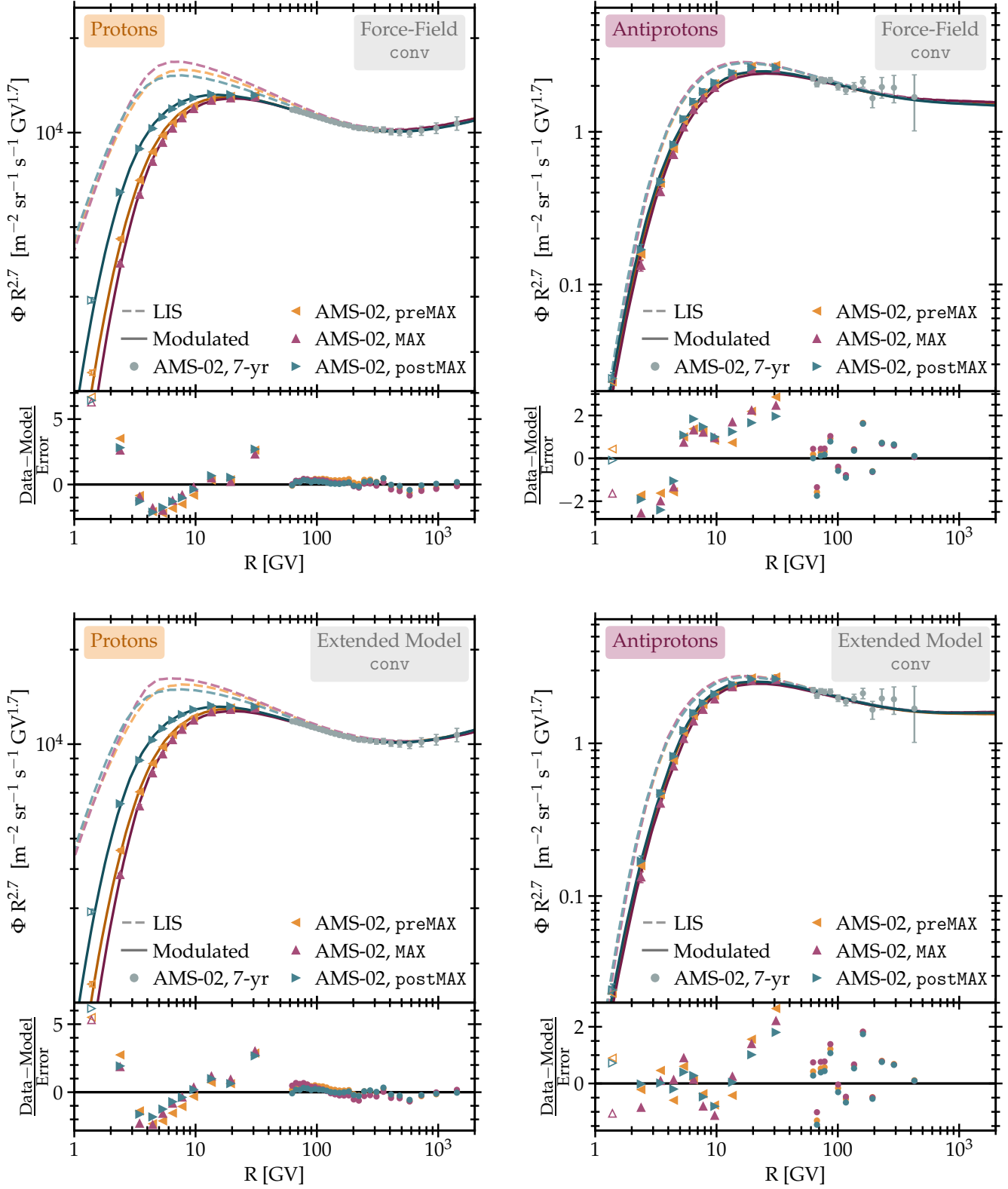


FIG. 4: The LIS spectra for protons (left panels) and antiprotons (right panels) using the force-field model (top panels) and extended force-field model (bottom panels) for solar modulation. The LISes are based on the conv propagation model.

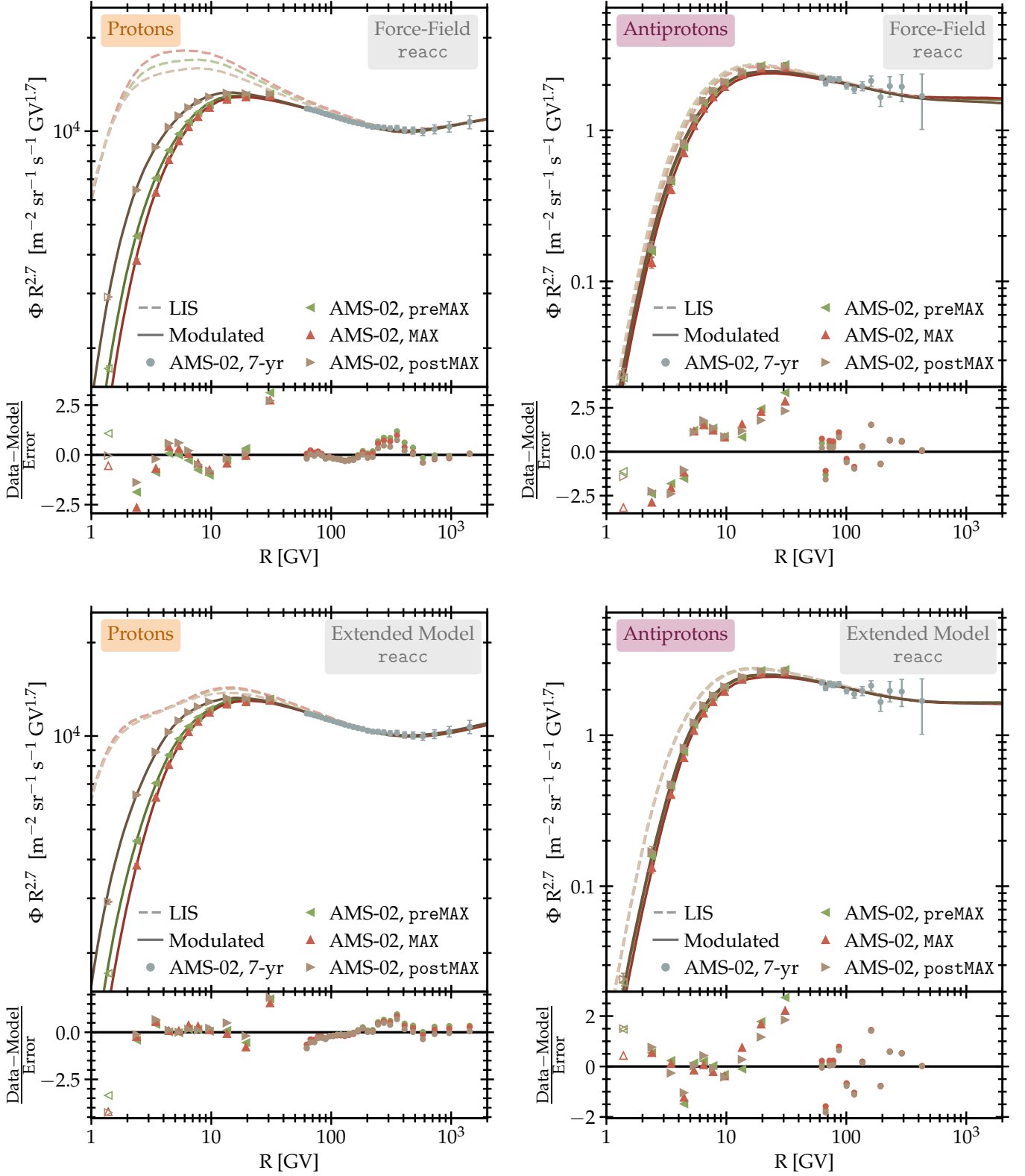


FIG. 5: The LIS spectra for protons (left panels) and antiprotons (right panels) using the force-field model (top panels) and extended force-field model (bottom panels) for solar modulation. The LISes are based on the reacc propagation model.

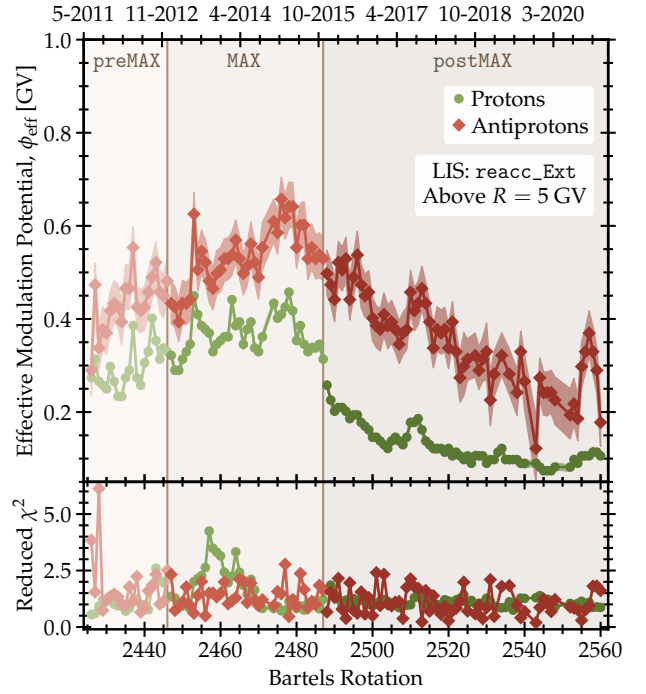
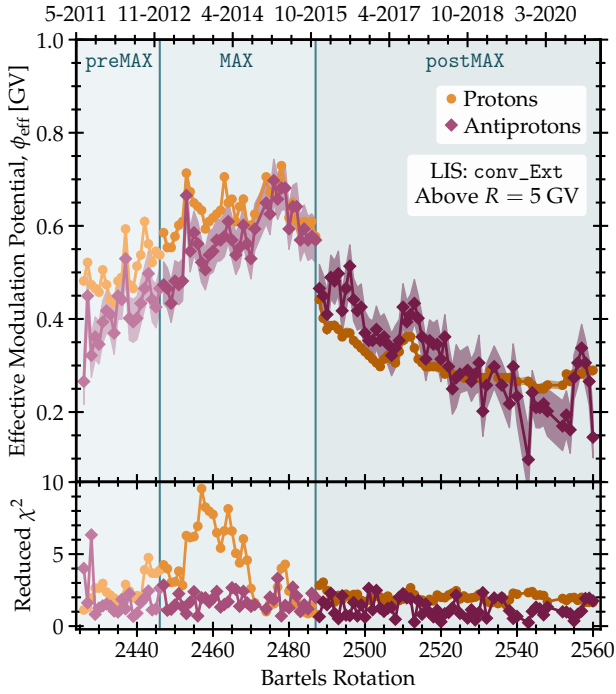
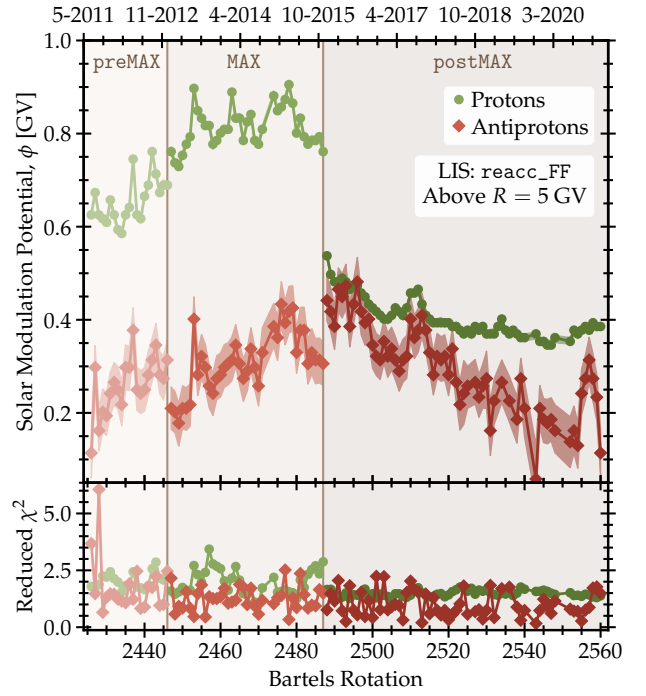
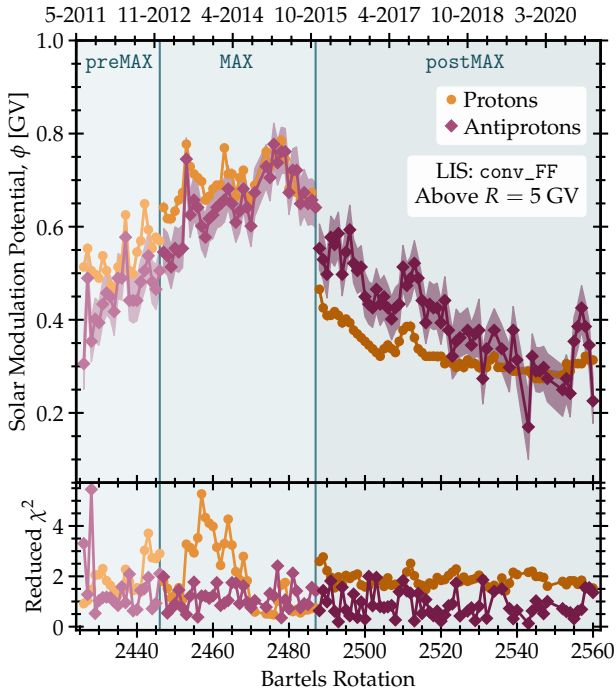


FIG. 6: The effective force-field solar modulation potential for each Bartels rotation for protons (shades of orange, circle markers) and antiprotons (shades of burgundy, diamond markers) for the three periods in the conv propagation model. Lighter, medium and darker shades indicate the **preMAX**, **MAX** and **postMAX** phase, respectively; note that the LIS differs in each period. Shaded bands around the data correspond to the 1σ uncertainty bands. The top panel employs the force-field (FF) fit LISes and the bottom panel the extended model (Ext) LISes. The effective potential is determined using only data above 5 GV in order to reduce biases for the Ext case (see text for more details). The bottom panel of each plot shows the reduced χ^2 for protons and antiprotons.

FIG. 7: Same as Figure 6 but for the reacc propagation model. Protons are given in shades of green, circle markers and antiprotons in shades of red, diamond markers.

ton and antiproton potentials are similar in the `postMAX` phase, although we expect the antiproton potential to be larger. Nonetheless, both cases seem to overall follow the expected behaviour reasonably well. The bottom panels of each plot show the reduced χ^2 for protons and antiprotons, obtained for the modulation potential at each Bartels rotation. In both the force-field and extended modulation case, the reduced χ^2 strongly worsens for protons during the solar maximum, further emphasising the complexity of the heliospheric processes during this solar configuration, as well as the observations that the force-field approximation is insufficient during the solar maximum, even above 5 GV.

Fig. 7 is similar to Fig. 6 but shows the effective solar modulation potential for the `reacc` propagation model. It can be seen that in this case the results are completely at odds with expectations. In the force-field case the modulation potential for protons is always larger than that of antiprotons, in any time period, by large factors ranging from 2 to 3, even in the `MAX` phase. For the extended modulation scenario the situation is reversed with antiprotons being more strongly modulated than protons during the entire time period, in contradiction with expectations. Overall, both the force-field and extended modulation results seem problematic within the `reacc` propagation model. The proton modulation potential for the `conv` and `reacc` case are actually similar in the `postMAX` phase, which indicates that, at least in this period, the force-field modulation might still be a reasonable approximation, at least for protons. Overall, however, the force-field model seems inadequate when used in conjunction with the `reacc` propagation model. Furthermore, these unexpected results for the extended modulation model also confirm that the achieved fit is probably unphysical, as discussed above. We note nonetheless that in both cases the quality of the fit is good, as can be seen from the bottom panels showing the reduced χ^2 . The unphysical result thus does not seem to come from a poor quality of the fit but from a complex interplay and degeneracy between several processes dominant at GeV energies, in particular solar modulation and re-acceleration, which the fit is not able to separate well.

For comparison, we also show the time-evolution of the solar modulation potentials for the 7-yr time-integrated models in Appendix B.

To further illustrate the above issues, Figures 8 to 10 show the probability distribution functions (PDFs) of a few select parameters that are especially inconsistent between the propagation models and time periods. Each figure shows the PDF for the three 7-year time-integrated solar modulation models (top panels), the three time-dependent fits with the force-field (`FF`) model (middle panels), and the three time-dependent fits with the extended (`Ext`) model (bottom panels). We note that in the 7-year time-integrated models, it is not necessarily expected that the parameters are consistent as the underlying solar modulation models are different. However, for the time-dependent fits, which use the same propaga-

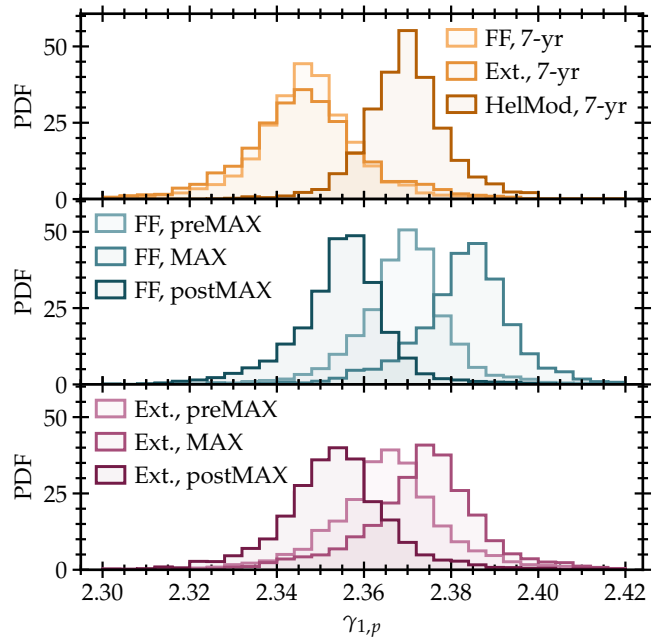


FIG. 8: Probability distribution from the Bayesian fit for the proton injection index $\gamma_{1,p}$, in the `conv` propagation model. Top panel shows the 7-yr time-integrated fits for the force-field (`FF`), extended (`Ext.`) and `HelMod` solar modulation models. Middle and bottom panels show the fits to the force-field and extended model for the three time periods, respectively.

tion and modulation models, parameters should be consistent, and a failure of this points towards systematic inconsistencies with the underlying modulation model and/or propagation model. In Table II, we list the difference between the PDFs from Figs. 8 to 10 in terms of σ . We calculate the significances by approximating each distribution as a Gaussian and checking the compatibility between the differences of a set of two distributions with zero, using error propagation.

Fig. 8 presents the proton injection spectral index, $\gamma_{1,p}$ in the `conv` model. The force-field fit shows a significant inconsistency, at a level of 4.22σ (see Tab. II), between the `MAX` and `postMAX` values, confirming that the force-field approximation breaks down during the `MAX` phase. The values of the `preMAX` and `postMAX` phases, when the force-field approximation works better, are in a more reasonable agreement, although still in tension at a 2σ level. For the extended modulation case, the agreement is generally better, although the `MAX` and `postMAX` values are still in tension at a 2.8σ level.

Figs. 9 and 10 show the PDFs of the proton injection spectral index, $\gamma_{1,p}$, and the Alfvén velocity, v_A , for the `reacc` model, respectively. A similar trend as above can be observed. In the extended modulation scenario, the PDFs show a very good consistency among the different time periods. However, this is at the price of unphysical values for the modulation potential and the LIS, as discussed previously. Conversely, for the force-field case, we again see a divergence among the values in the differ-

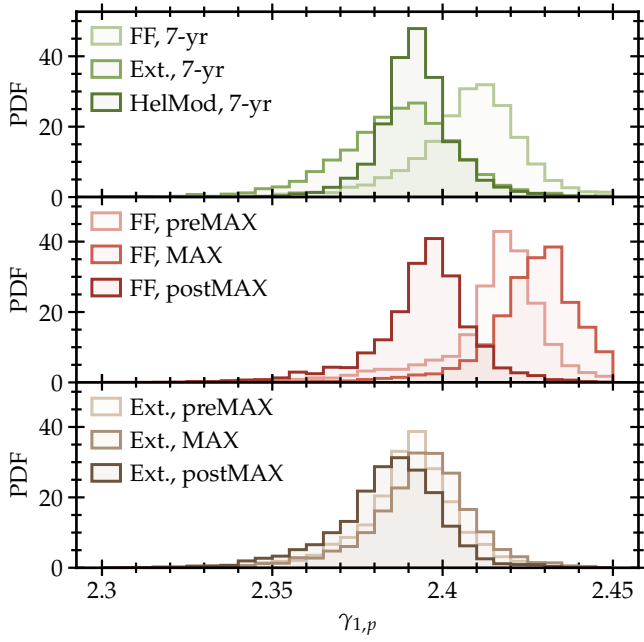


FIG. 9: Same as Fig. 8, but for the **reacc** propagation model.

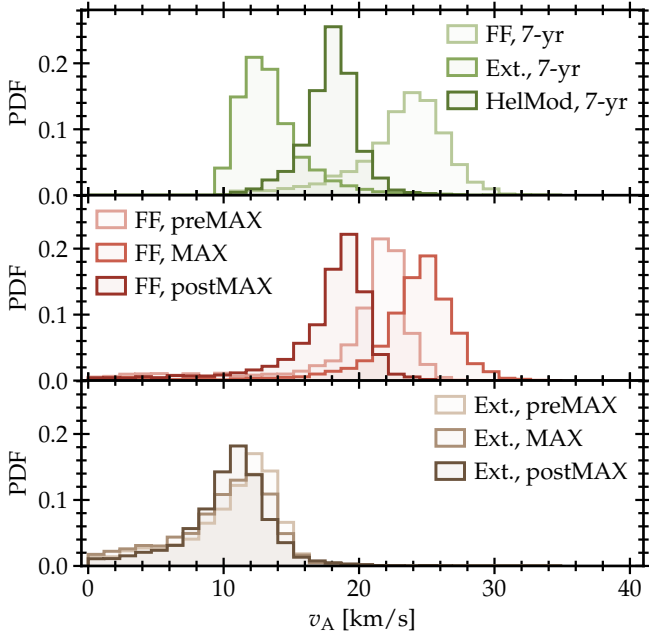


FIG. 10: Probability distribution from the Bayesian fit for the Alfvén velocity, v_A , in the **reacc** propagation model. Top panel shows the 7-yr time-integrated fits for the force-field (FF), extended (Ext.) and HelMod solar modulation models. Middle and bottom panels show the fits to the force-field and extended model for the 3 time periods, respectively.

ent time periods at a level up to 3.5σ for the **postMAX** and **MAX** cases. This once more confirms that in the **reacc** propagation model, the force-field solar modulation model fails to provide a consistent picture.

$\gamma_{1,p}$	conv	7-yr	FF \leftrightarrow Ext:	0.11σ
			FF \leftrightarrow HelMod:	2.96σ
			Ext \leftrightarrow HelMod:	3.03σ
	FF		preMAX \leftrightarrow MAX:	2.27σ
			MAX \leftrightarrow postMAX:	4.22σ
			preMAX \leftrightarrow postMAX:	1.98σ
Ext		preMAX \leftrightarrow MAX:	1.18σ	
		MAX \leftrightarrow postMAX:	2.82σ	
		preMAX \leftrightarrow postMAX:	1.63σ	
v_A	reacc	7-yr	FF \leftrightarrow Ext:	1.53σ
			FF \leftrightarrow HelMod:	0.03σ
			Ext \leftrightarrow HelMod:	2.25σ
	FF		preMAX \leftrightarrow MAX:	1.17σ
			MAX \leftrightarrow postMAX:	3.83σ
			preMAX \leftrightarrow postMAX:	2.81σ
Ext		preMAX \leftrightarrow MAX:	0.37σ	
		MAX \leftrightarrow postMAX:	0.67σ	
		preMAX \leftrightarrow postMAX:	0.33σ	

TABLE II: Summary of the differences in PDFs of Figs. 8, 9 and 10. The first column indicates the parameter, second column the propagation model, third column the solar modulation model, *i.e.* either for time-integrated 7-yr fits or force-field (FF) and extended model (Ext), and last column lists the significance σ of the tension between two distributions as indicated.

VI. SUMMARY AND CONCLUSIONS

We conduct detailed fits of cosmic-ray propagation to the latest time-dependent AMS-02 data and study the impact of the chosen solar modulation model on the parameters of the propagation model. The AMS-02 data provides cosmic-ray fluxes over a full solar cycle at each Bartels rotation. Crucially, this includes cosmic-ray antiprotons, which differ from other cosmic-ray nuclei in two ways: They are the only negatively charged cosmic-ray nuclei, which makes them an important and com-

plementary probe of the charge sign-dependence of solar modulation. Furthermore, the spectral shape of their fluxes is unique, as they are only produced as secondaries in inelastic scattering processes.

We consider two propagation scenarios, one focused on convection, dubbed `conv`, and one on re-acceleration, dubbed `reacc`, and three solar modulation models: the standard force-field, an extended force-field, where the modulation potential differs above and below a rigidity break at a few GV, and `HelMod`. Furthermore, we divide the solar cycle into three time periods: (1) before the solar maximum of cycle 24 in 2014-2015 (`preMAX`), (2) during the maximum (`MAX`), and (3) after the solar maximum (`postMAX`). We study these periods separately, allowing us to examine the consistency between the individual results. Our findings can be summarized as follows:

- In the `conv` propagation model for positively charged particles, the extended force-field modulation provides consistent modulation potentials below and above the break for phases of moderate to low solar activity, resembling a force field. This indicates that the force-field approximation can describe the modulation of positively charged nuclei relatively well during off-maximum phases of solar activity. On the other hand, during solar maximum, we detect a significant difference in the low and high potential in the extended model (see Tab. I), indicating that the force-field approximation is not appropriate during this period. This is also confirmed by a strong worsening in the fit quality during the solar maximum when the spectra are compared to the data for each Bartels rotation (see more below).
- For antiprotons, we detect strong differences in the low and high potential in the extended model during all solar phases, *i.e.*, during both the maximum and minimum solar activity phases. We ascribe this result to two possible causes: (1) An incorrect antiproton LIS due to a combination of incorrect propagation models and/or uncertainties in the antiproton production cross section, with solar modulation trying to compensate for this. (2) A true failure of the force-field approximation, perhaps related to the peculiar, peak-shaped, spectrum of antiprotons, as opposed to the power-law-like shape for the other nuclei (see Fig. 3).
- For the `reacc` propagation scenario, the conclusions are very different. The low and high potential of the extended modulation model strongly differ throughout each solar period, both for protons and antiprotons. This, in principle, would indicate that the force-field approximation is always inadequate, even during low solar activity periods. However, we believe that this is rather due to an unphysical result achieved by the best-fit. This seems to be confirmed by the shape of the LIS, which is very

different with respect to the case of the `conv` model (see Figs. 4 and 5), as well as by the properties of the time-dependent modulation potentials (see Figs. 6 and 7), which is at odds with expectations, as further discussed below. This seems to point towards difficulties of the fitting procedure to disentangle solar modulation and re-acceleration, which both act in a similar way at similar rigidities.

- For a given propagation and solar modulation model, the LIS fluxes must always be the same, independently of solar activity, as we do not expect time-dependent changes in the (nearby) Galactic propagation on short time scales. In the force-field approximation, for both propagation scenarios, we find that the LIS fluxes obtained in each of the three time periods show discrepancies by about 10–20%. When excluding the solar maximum and comparing only periods of low or moderate solar activity this discrepancy is still at the level of 10 – 15%. This persists when using the extended solar modulation model, indicating that, at the moment, the solar modulation-related systematic uncertainty in the reconstructed LIS and propagation parameters is at least at the level of 10 – 15%.

Looking at specific parameters confirms the above conclusions. For example, the proton injection spectral index, $\gamma_{1,p}$, and the Alfvén velocity, v_A , show differences at the $\sim 4\sigma$ level between the values determined in the three time periods within the force-field approximation. Conversely, the discrepancy goes down to a more reasonable $\sim 1-2\sigma$ when the solar maximum period is excluded, or when the extended solar modulation is employed (see Figs. 8 to 10 and Tab. II).

- A further tool to evaluate the systematic uncertainties related to solar modulation is the temporal behaviour of the modulation itself. Given the LIS derived for each fit that we performed, we have calculated the effective force-field modulation potential as function of time for each Bartels rotation (see Figs. 6 and 7). Based on our current understanding of cosmic-ray propagation in the solar system, and from the behaviour of the time-dependent AMS-02 data, we expect that solar modulation for protons and antiprotons should be comparable during times of maximum solar activity, larger for protons before the maximum of solar cycle 24 and larger for antiprotons after the maximum.

While the temporal behaviour of the solar modulation potential in the `conv` propagation model is somewhat consistent with these expectations, the results in the `reacc` model are incompatible with our understanding of heliospheric propagation, for both the force-field and the extended modulation case. Thus, these effective solar modulation models are generally unable to disentangle the degeneracies between solar modulation itself and other

low-energy processes, such as re-acceleration, which might only be achievable with more sophisticated heliospheric propagation models such as `HelMod`.

- Using the `HelMod` modulation, we obtain similar LIS fluxes (see Figs. 2 and A.1) and time-dependent potentials (see Figs. B.1 and B.2) for both the `conv` and `reacc` scenarios. This is probably not surprising since we use a fixed modulation without free parameters as tuned in [14, 15, 71], which means that the LIS is basically fixed. We stress however, that a self-consistent analysis would require to re-derive and re-tune the `HelMod` modulation together with Galactic propagation. This is, however, a task that requires a dedicated study which we leave for future works.

Our work shows that our current modelling of solar modulation introduces significant systematic uncertainties of at least at a level of 10 – 15%, in the reconstruction of cosmic-ray LIS fluxes and Galactic propagation models. These uncertainties originate both from an interplay with processes at low energies, such as re-acceleration, that are degenerate with solar modulation effects, and from difficulties in correctly modelling solar modulation in the different phases of the solar activity cycle, in par-

ticular during the solar maximum.

Together with the uncertainties related to nuclear cross sections, this is significantly limiting our ability to perform precise cosmic-ray physics at the percent-level precision which is otherwise achieved by the AMS-02 measurements. Future data, in particular time-dependent data spanning a full 22-year solar cycle covering both polarity configurations of the Sun’s magnetic field will be crucial to improve our knowledge of cosmic-ray propagation in the solar system, and reduce these uncertainties.

ACKNOWLEDGEMENTS

Many thanks to Stefano Della Torre for helpful discussions on `HelMod`. I.J. and A.C. acknowledge support from the Research grant TAsP (Theoretical Astroparticle Physics) funded by INFN, and Research grant “Addressing systematic uncertainties in searches for dark matter”, Grant No. 2022F2843L, CUP D53D23002580006 funded by the Italian Ministry of University and Research (MUR). M.D.M. acknowledges support from the Italian Ministry of University and Research (MUR), PRIN 2022 “EXSKALIBUR – Euclid-Cross-SKA: Likelihood Inference Building for Universe’s Research”, Grant No. 20222BBYB9, CUP I53D23000610 0006, and from the European Union – Next Generation EU.

-
- [1] M. S. Potgieter, *Living Reviews in Solar Physics* **10**, 3 (2013), [arXiv:1306.4421 \[physics.space-ph\]](#).
 - [2] J. S. Rankin, V. Bindi, A. M. Bykov, A. C. Cummings, S. Della Torre, V. Florinski, B. Heber, M. S. Potgieter, E. C. Stone, and M. Zhang, *Space Sci. Rev.* **218**, 42 (2022).
 - [3] E. N. Parker, *The Astrophysical Journal* **128**, 664 (1958).
 - [4] E. N. Parker, *Planetary and Space Science* **13**, 9 (1965).
 - [5] J. R. Jokipii, *Reviews of Geophysics and Space Physics* **9**, 27 (1971).
 - [6] I. G. Usoskin, A. Gil, G. A. Kovaltsov, A. L. Mishev, and V. V. Mikhailov, *J. Geophys. Res. Space Phys.* **122**, 3875 (2017), [arXiv:1705.07197 \[physics.space-ph\]](#).
 - [7] B.-B. Wang, X.-J. Bi, K. Fang, S.-J. Lin, and P.-F. Yin, *Phys. Rev. D* **100**, 063006 (2019), [arXiv:1904.03747 \[astro-ph.HE\]](#).
 - [8] C. Corti, V. Bindi, C. Consolandi, and K. Whitman, *Astrophys. J.* **829**, 8 (2016), [arXiv:1511.08790 \[astro-ph.HE\]](#).
 - [9] M. Kuhlen and P. Mertsch, *Phys. Rev. Lett.* **123**, 251104 (2019), [arXiv:1909.01154 \[astro-ph.HE\]](#).
 - [10] N. Tomassetti, *Phys. Rev. D* **96**, 103005 (2017), [arXiv:1707.06917 \[astro-ph.HE\]](#).
 - [11] N. Tomassetti, B. Bertucci, E. Fiandrini, and B. Khiali, *Galaxies* **13**, 23 (2025), [arXiv:2503.14025 \[astro-ph.HE\]](#).
 - [12] N. Tomassetti, F. Barão, B. Bertucci, E. Fiandrini, J. Figueiredo, J. Barreira, and M. Orcinha, *Phys. Rev. Lett.* **121**, 251104 (2018), [arXiv:1811.08909 \[astro-ph.HE\]](#).
 - [13] H.-M. Zhang, S.-J. Lin, J. Feng, J.-T. Jiang, and L.-L. Yang, (2026), [arXiv:2601.07649 \[astro-ph.HE\]](#).
 - [14] M. J. Boschini *et al.*, *Astrophys. J.* **840**, 115 (2017), [arXiv:1704.06337 \[astro-ph.HE\]](#).
 - [15] M. J. Boschini *et al.*, *Astrophys. J.* **858**, 61 (2018), [arXiv:1804.06956 \[astro-ph.HE\]](#).
 - [16] A. Cuoco, M. Krämer, and M. Korsmeier, *Phys. Rev. Lett.* **118**, 191102 (2017), [arXiv:1610.03071 \[astro-ph.HE\]](#).
 - [17] F. Calore, M. Cirelli, L. Derome, Y. Genolini, D. Maurin, P. Salati, and P. D. Serpico, *SciPost Phys.* **12**, 163 (2022), [arXiv:2202.03076 \[hep-ph\]](#).
 - [18] L. Bergstrom, T. Bringmann, I. Cholis, D. Hooper, and C. Weniger, *Phys. Rev. Lett.* **111**, 171101 (2013), [arXiv:1306.3983 \[astro-ph.HE\]](#).
 - [19] I. John and T. Linden, *JCAP* **12**, 007 (2021), [arXiv:2107.10261 \[astro-ph.HE\]](#).
 - [20] E. C. Stone, A. C. Cummings, F. B. McDonald, B. C. Heikkila, N. Lal, and W. R. Webber, *Science* **341**, 1236408 (2013).
 - [21] F. Clette and L. Lefèvre, “Silso sunspot number v2.0,” <https://doi.org/10.24414/qnza-ac80> (2015), published by WDC SILSO - Royal Observatory of Belgium (ROB).
 - [22] M. Aguilar *et al.* (AMS), *Phys. Rev. Lett.* **134**, 051002 (2025).
 - [23] M. Aguilar *et al.* (AMS), *Phys. Rev. Lett.* **134**, 051001 (2025).
 - [24] O. Adriani *et al.*, *The Astrophysical Journal* **765**, 91 (2013).

- [25] O. Adriani *et al.*, *Astrophys. J.* **810**, 142 (2015), arXiv:1512.01079 [astro-ph.SR].
- [26] O. Adriani *et al.*, *Phys. Rev. Lett.* **116**, 241105 (2016), arXiv:1606.08626 [astro-ph.HE].
- [27] K. C. Y. Ng, J. F. Beacom, A. H. G. Peter, and C. Rott, *Phys. Rev. D* **94**, 023004 (2016), arXiv:1508.06276 [astro-ph.HE].
- [28] T. Linden, J. F. Beacom, A. H. G. Peter, B. J. Buckman, B. Zhou, and G. Zhu, *Phys. Rev. D* **105**, 063013 (2022), arXiv:2012.04654 [astro-ph.HE].
- [29] T. Linden, J.-T. Li, B. Zhou, I. John, M. Crnogorčević, A. H. G. Peter, and J. F. Beacom, *Phys. Rev. D* **112**, 103030 (2025), arXiv:2505.04625 [astro-ph.HE].
- [30] A. Acharyya *et al.*, *Astrophys. J. Lett.* **989**, L16 (2025), arXiv:2505.06348 [astro-ph.HE].
- [31] L. Maccione, *Phys. Rev. Lett.* **110**, 081101 (2013), arXiv:1211.6905 [astro-ph.HE].
- [32] R. Kappl, *Comput. Phys. Commun.* **207**, 386 (2016), arXiv:1511.07875 [astro-ph.SR].
- [33] M. J. Boschini, S. Della Torre, M. Gervasi, G. La Vacca, and P. G. Rancoita, *Adv. Space Res.* **70**, 2649 (2022).
- [34] L. J. Gleeson and W. I. Axford, *ApJ* **154**, 1011 (1968).
- [35] R. A. Caballero-Lopez and H. Moraal, *Journal of Geophysical Research: Space Physics* **109**, A01101 (2004).
- [36] J. Gieseler, B. Heber, and K. Herbst, *Journal of Geophysical Research: Space Physics* **122**, 10964 (2017).
- [37] I. Cholis, D. Hooper, and T. Linden, *Phys. Rev. D* **93**, 043016 (2016), arXiv:1511.01507 [astro-ph.SR].
- [38] I. Cholis, D. Hooper, and T. Linden, *JCAP* **10**, 051 (2022), arXiv:2007.00669 [astro-ph.HE].
- [39] J.-T. Li, J. F. Beacom, and A. H. G. Peter, *Astrophys. J.* **937**, 27 (2022), arXiv:2206.14815 [astro-ph.SR].
- [40] W.-C. Long and J. Wu, *Phys. Rev. D* **109**, 083009 (2024), arXiv:2403.20038 [astro-ph.SR].
- [41] C.-R. Zhu, *Astrophys. J.* **975**, 270 (2024), arXiv:2409.18389 [astro-ph.HE].
- [42] C.-R. Zhu and M.-J. Wang, *Astrophys. J.* **983**, 156 (2025), arXiv:2502.10016 [astro-ph.HE].
- [43] C.-R. Zhu and M.-J. Wang, *Astrophys. J.* **980**, 116 (2025), arXiv:2501.10922 [astro-ph.HE].
- [44] M. Aguilar *et al.* (AMS), *Phys. Rept.* **894**, 1 (2021).
- [45] O. Adriani *et al.* (CALET), *Phys. Rev. Lett.* **129**, 101102 (2022), arXiv:2209.01302 [astro-ph.HE].
- [46] F. Alemanno *et al.*, *Phys. Rev. Lett.* **126**, 201102 (2021), arXiv:2105.09073 [astro-ph.HE].
- [47] F. Alemanno *et al.* (DAMPE), *Sci. Bull.* **67**, 2162 (2022), arXiv:2210.08833 [astro-ph.HE].
- [48] M. Aguilar *et al.* (AMS), *Phys. Rev. Lett.* **132**, 261001 (2024).
- [49] D. Maurin *et al.*, *Phys. Rept.* **1161**, 1 (2026), arXiv:2503.16173 [astro-ph.HE].
- [50] N. Tomassetti, M. Orcinha, F. Barão, and B. Bertucci, *Astrophys. J. Lett.* **849**, L32 (2017), arXiv:1707.06916 [astro-ph.HE].
- [51] N. Tomassetti, B. Bertucci, and E. Fiandrini, *Phys. Rev. D* **106**, 103022 (2022), arXiv:2210.05693 [astro-ph.SR].
- [52] A. Cuoco, J. Heisig, L. Klamt, M. Korsmeier, and M. Krämer, *Phys. Rev. D* **99**, 103014 (2019), arXiv:1903.01472 [astro-ph.HE].
- [53] M. Korsmeier and A. Cuoco, *Phys. Rev. D* **103**, 103016 (2021), arXiv:2103.09824 [astro-ph.HE].
- [54] M. Korsmeier and A. Cuoco, *Phys. Rev. D* **105**, 103033 (2022), arXiv:2112.08381 [astro-ph.HE].
- [55] M. Di Mauro, F. Donato, M. Korsmeier, S. Mancini, and L. Orusa, *Phys. Rev. D* **108**, 063024 (2023), arXiv:2304.01261 [astro-ph.HE].
- [56] M. Di Mauro, M. Korsmeier, and A. Cuoco, *Phys. Rev. D* **109**, 123003 (2024), arXiv:2311.17150 [astro-ph.HE].
- [57] A. W. Strong and I. V. Moskalenko, *Astrophys. J.* **509**, 212 (1998), arXiv:astro-ph/9807150.
- [58] A. W. Strong, (2015), arXiv:1507.05020 [astro-ph.HE].
- [59] F. Feroz, M. P. Hobson, and M. Bridges, *Mon. Not. Roy. Astron. Soc.* **398**, 1601 (2009), arXiv:0809.3437 [astro-ph].
- [60] M. di Mauro, F. Donato, A. Goudelis, and P. D. Serpico, *Phys. Rev. D* **90**, 085017 (2014), [Erratum: *Phys. Rev. D* **98**, 049901 (2018)], arXiv:1408.0288 [hep-ph].
- [61] F. Donato, M. Korsmeier, and M. Di Mauro, *Phys. Rev. D* **96**, 043007 (2017), arXiv:1704.03663 [astro-ph.HE].
- [62] M. Korsmeier, F. Donato, and M. Di Mauro, *Phys. Rev. D* **97**, 103019 (2018), arXiv:1802.03030 [astro-ph.HE].
- [63] Y. Genolini, D. Maurin, I. V. Moskalenko, and M. Unger, *Phys. Rev. C* **98**, 034611 (2018), arXiv:1803.04686 [astro-ph.HE].
- [64] Y. Génolini, D. Maurin, I. V. Moskalenko, and M. Unger, *Phys. Rev. C* **109**, 064914 (2024), arXiv:2307.06798 [astro-ph.HE].
- [65] L. O. Drury and A. W. Strong, *Astron. Astrophys.* **597**, A117 (2017), arXiv:1608.04227 [astro-ph.HE].
- [66] E. E. Vos and M. S. Potgieter, *The Astrophysical Journal* **815**, 119 (2015).
- [67] J. R. Jokipii, E. H. Levy, and W. B. Hubbard, *The Astrophysical Journal* **213**, 861 (1977).
- [68] M. Aguilar *et al.*, *Physical Review Letters* **121**, 051101 (2018).
- [69] M. J. Boschini, S. Della Torre, M. Gervasi, G. La Vacca, and P. G. Rancoita, *Adv. Space Res.* **62**, 2859 (2018), arXiv:1704.03733 [astro-ph.SR].
- [70] M. J. Boschini, S. Della Torre, M. Gervasi, G. La Vacca, and P. G. Rancoita, *Adv. Space Res.* **64**, 2459 (2019), arXiv:1903.07501 [physics.space-ph].
- [71] M. J. Boschini *et al.*, *Astrophys. J. Suppl.* **250**, 27 (2020), arXiv:2006.01337 [astro-ph.HE].
- [72] I. Cholis, T. Linden, and D. Hooper, *Phys. Rev. D* **99**, 103026 (2019), arXiv:1903.02549 [astro-ph.HE].
- [73] M.-Y. Cui, Q. Yuan, Y.-L. S. Tsai, and Y.-Z. Fan, *Phys. Rev. Lett.* **118**, 191101 (2017), arXiv:1610.03840 [astro-ph.HE].
- [74] K.-K. Duan, X. Wang, W.-H. Li, Z.-H. Xu, Y.-L. S. Tsai, and Y.-Z. Fan, (2025), arXiv:2506.13352 [astro-ph.CO].
- [75] M. Cirelli, D. Gaggero, G. Giesen, M. Taoso, and A. Urbano, *JCAP* **12**, 045 (2014), arXiv:1407.2173 [hep-ph].
- [76] O. Adriani *et al.*, *Physical Review Letters* **105** (2010), 10.1103/physrevlett.105.121101.
- [77] O. Adriani *et al.*, *Pisma Zh. Eksp. Teor. Fiz.* **96**, 693 (2012).

Appendix A: Further LIS and Modulated Fluxes of Cosmic-Ray Nuclei

Figure A.1 is similar to Fig. 2 but for the reacc propagation model, showing the cosmic-ray fluxes for our 7-year time-integrated fits with the force-field (orange), extended (burgundy) and He1Mod (green) solar modulations models. The agreement with the data is similar to the

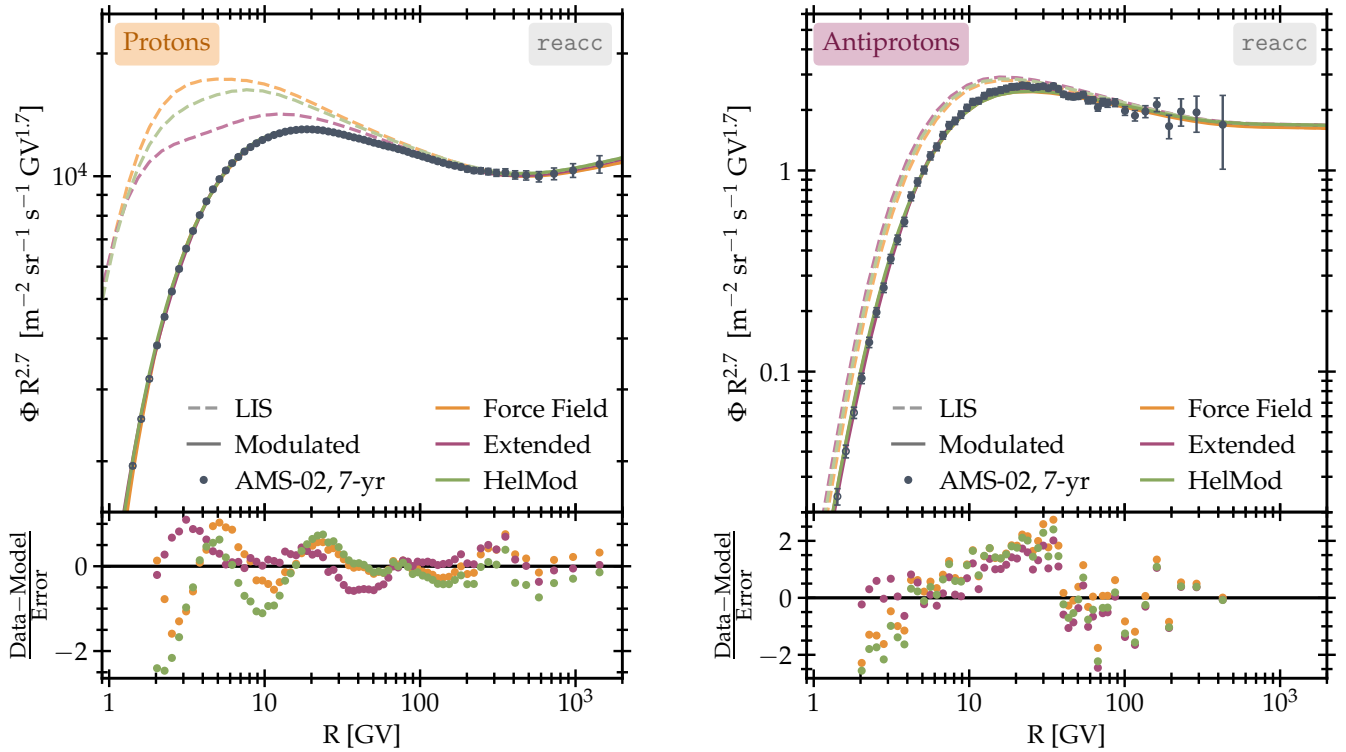


FIG. A.1: The spectra for protons (left panel) and antiprotons (right panel) for the 7-year time-integrated fit in the `reacc` model. In each plot, the LIS (dashed line) and modulated flux (solid) line are given for a different solar-modulation model: the force-field potential (orange), the extended force-field potential (burgundy) and the `HelMod` model (green). The residuals in each plot are compared to the 7-yr time-integrated AMS-02 data.

conv case with the residuals at a level of $\sim 1 - 2\sigma$. The main difference is a larger spread in the proton LIS fluxes, mainly due to the LIS of the extended model differing the most from the other two. This LIS is similar to the one obtained in time-dependent fits and is further discussed in the main text.

Figures A.2 to A.5 show the LIS and modulated fluxes for all cosmic-ray nuclei and ratios that are fitted in our analysis for the three time periods (see the main text for protons and antiprotons). Figs. A.2 and A.3 present the fluxes in the `conv` propagation model with the force-field and extended solar modulation model, respectively, while Figs. A.4 and A.5 show the fluxes in the `reacc` propagation model with the force-field and extended solar modulation model, respectively. The time-dependent AMS-02 data is complemented with the 7-year time-integrated data at higher rigidities (light grey circle markers). Note that in some cases, only time-dependent fluxes are available, as in the Helium-3-to-Helium-4 and Boron-to-Helium ratios, or only time-integrated data is available, as in the case of the Boron-to-Carbon and antiproton-to-proton ratios, where we only include the data above which no time-dependent data is available (see Section II for details). Data that is not included in the fit is indicated by empty markers. In general the quality of the fit is good in all cases, as indicated by the residuals which are at the level of $\sim 1 - 2\sigma$.

Appendix B: Time-Independent Solar Modulation Potential

Figures B.1 and B.2 show the change in the effective force-field solar modulation potential for each Bartels rotation for protons and antiprotons. Each panel refers to a different LIS relative to the 7-yr AMS-02 dataset fit for the two propagation models (`conv` and `reacc`) and the three solar modulation models (force-field, extended force-field and `HelMod`). The shaded bands around the data points correspond to the 1σ uncertainty bands. In all plots, the reduced χ^2 is typically the worst during the solar maximum, indicating that this period is especially hard to model. Beside the AMS-02 data we also use PAMELA data to cover the solar minimum at around 2008. In particular, we use the time-dependent proton data from [24]. Unfortunately, no time-dependent antiproton data from PAMELA is available. Instead, we use the two published time-integrated datasets, covering the period from July 2006 to December 2008 [76], and from July 2006 to December 2009 [77], respectively. Note that the LIS fluxes are only obtained from the fit to AMS-02 data. Nonetheless, we believe that a comparison of the time-dependent potentials to the PAMELA time period is still insightful.

Regarding the `conv` propagation model results, shown in Fig. B.1, it can be seen that the force-field and ex-

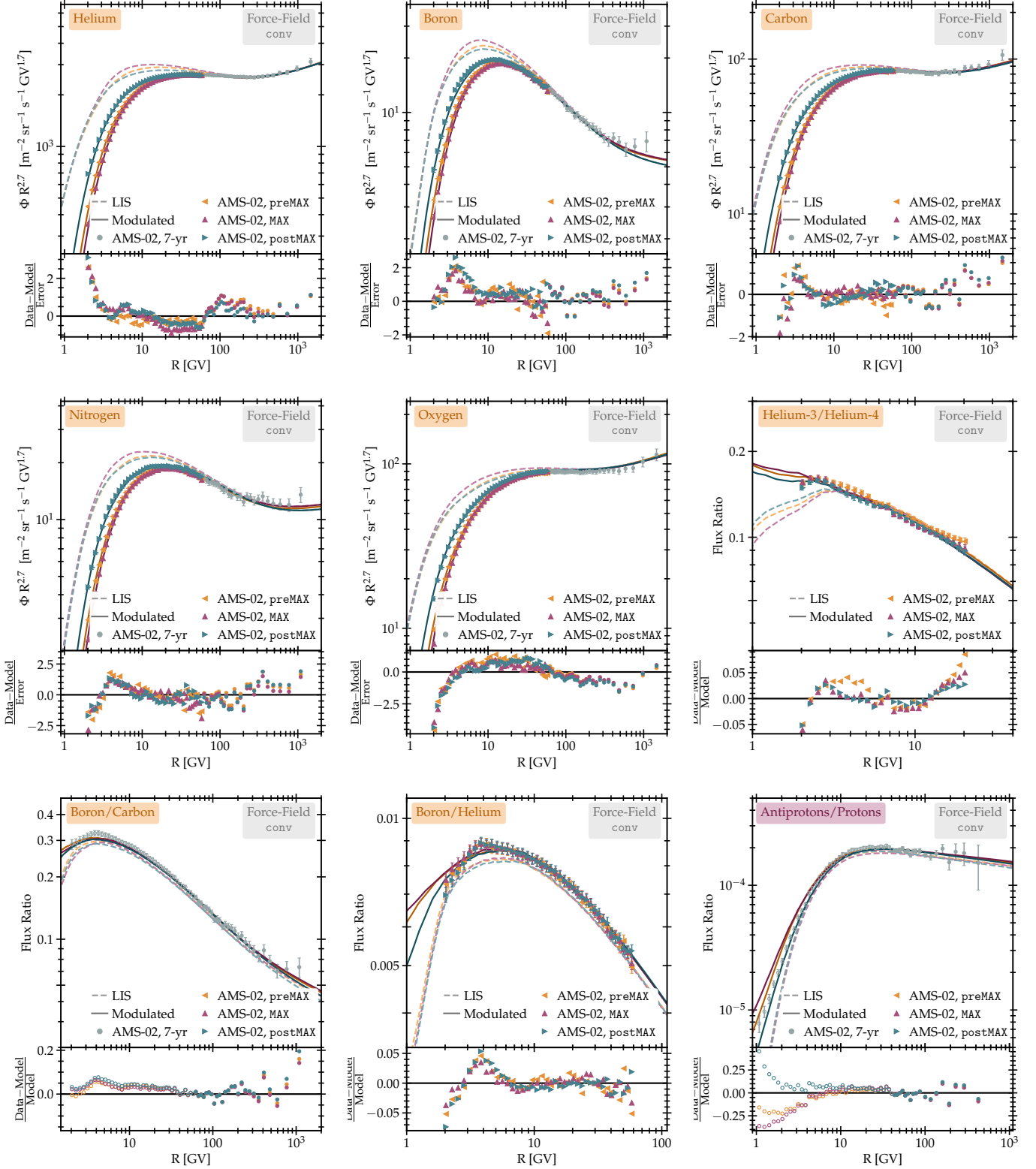


FIG. A.2: Similar to Fig. 4, the LIS and modulated fluxes of the fits to the 3 time-periods for the conv propagation and force-field modulation model. Note that for the Boron/Carbon and antiproton/proton no time-dependent data is available.

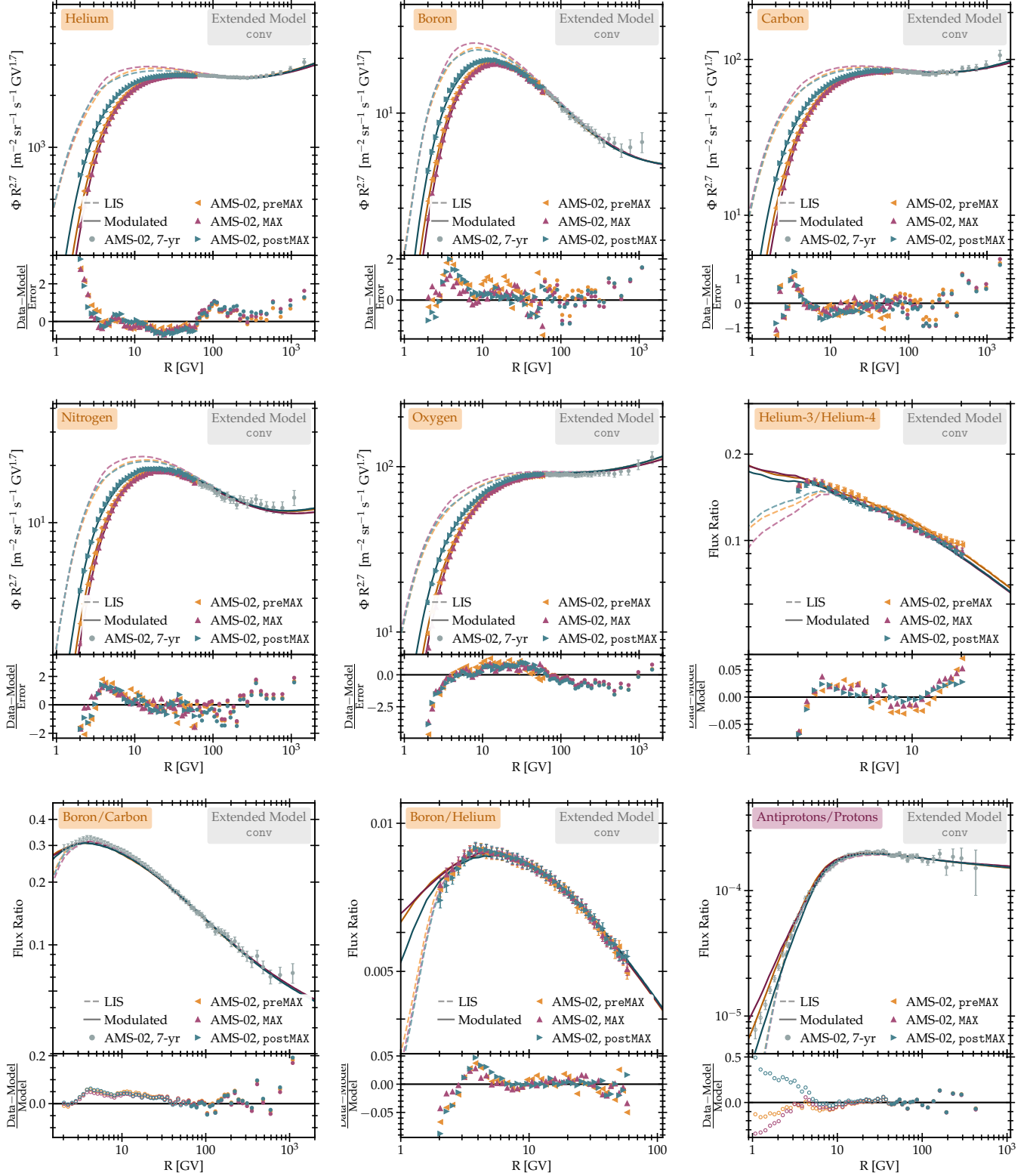


FIG. A.3: Similar to Fig. 4, the LIS and modulated fluxes of the fits to the 3 time-periods for the conv propagation and extended modulation model. Note that for the Boron/Carbon and antiproton/proton no time-dependent data is available.

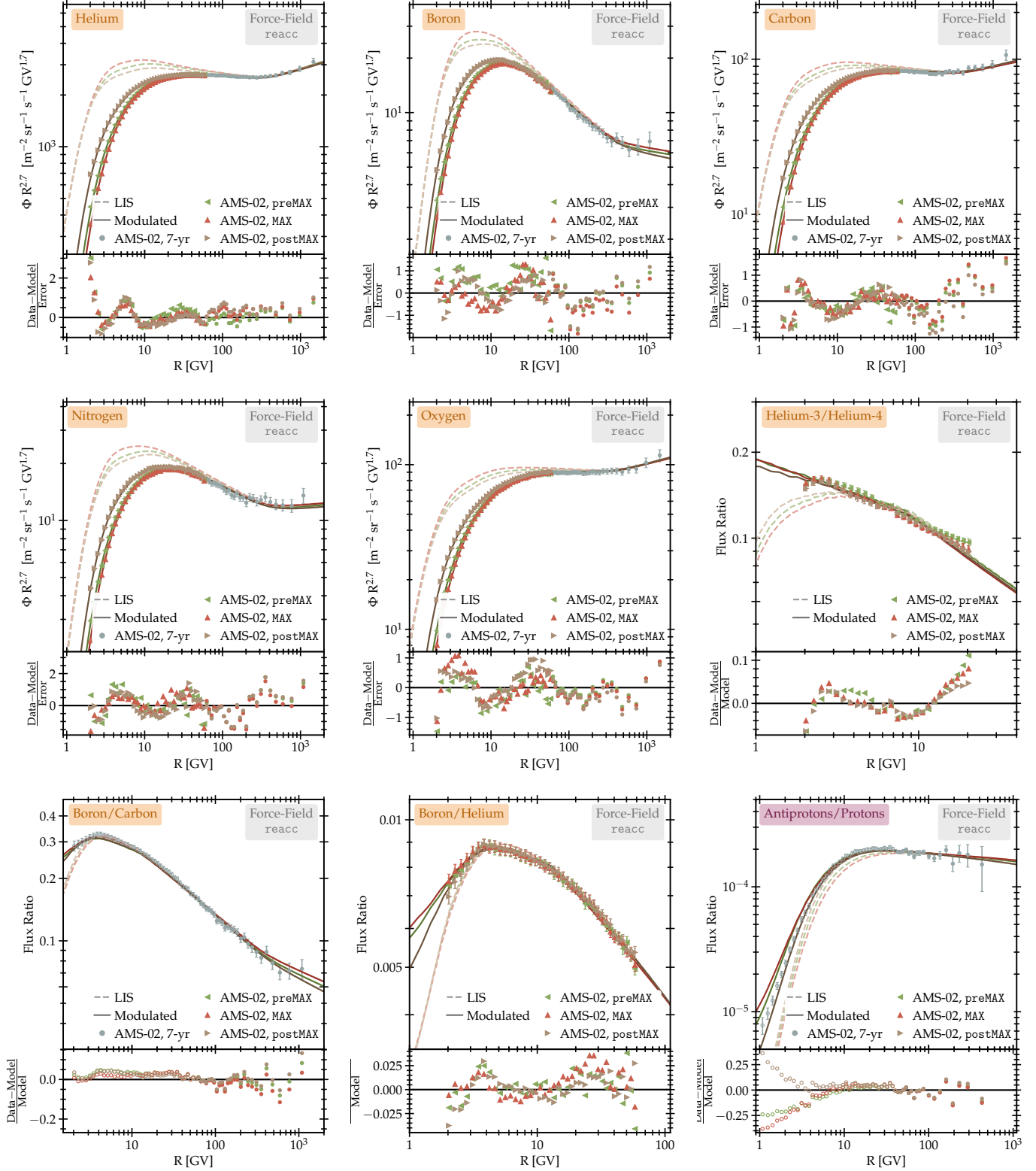


FIG. A.4: Similar to Fig. 5, the LIS and modulated fluxes of the fits to the 3 time-periods for the reacc propagation and force-field modulation model. Note that for the Boron/Carbon and antiproton/proton no time-dependent data is available.

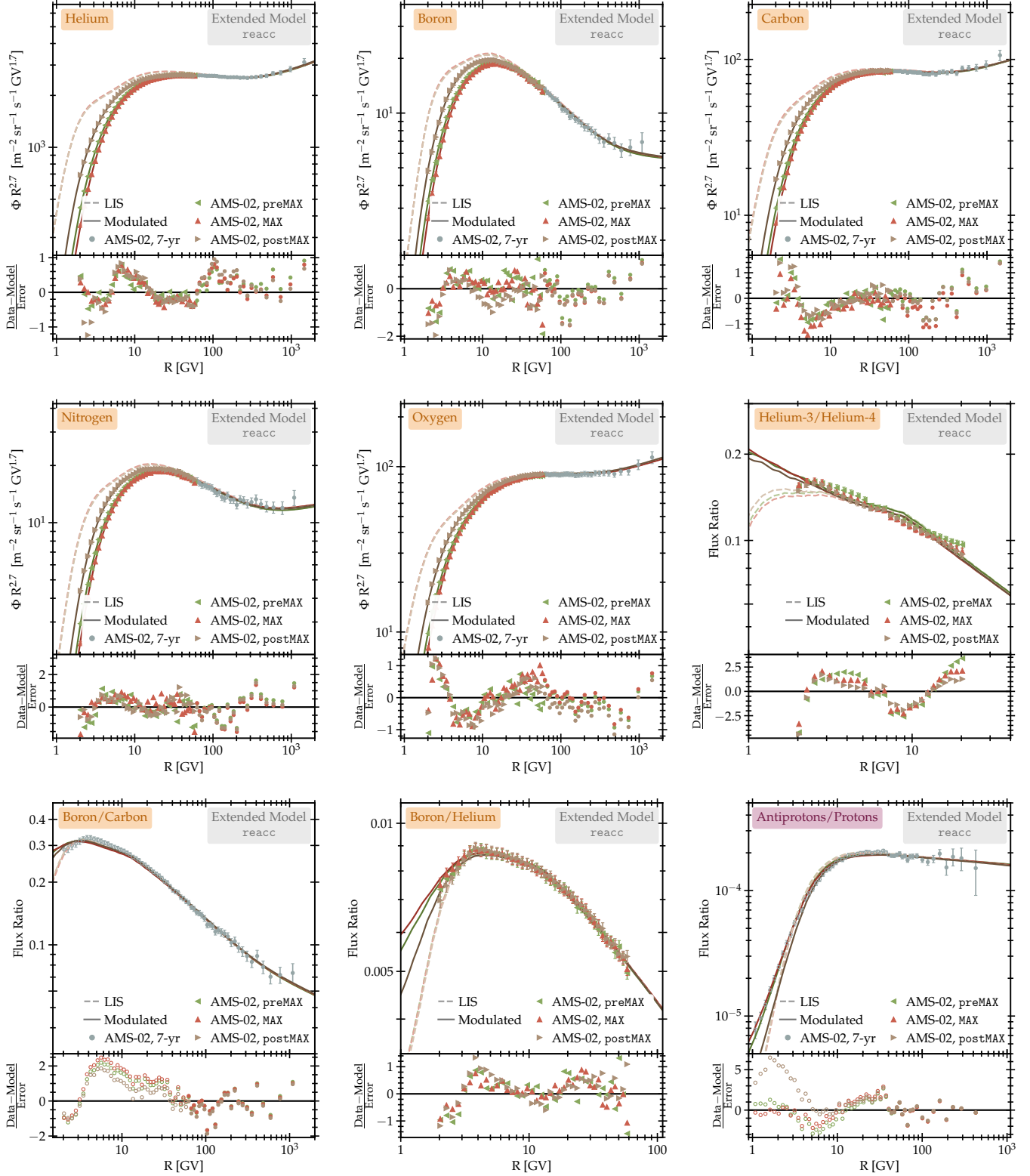


FIG. A.5: Similar to Fig. 5, the LIS and modulated fluxes of the fits to the 3 time-periods for the `reacc` propagation and extended modulation model. Note that for the Boron/Carbon and antiproton/proton no time-dependent data is available.

tended modulation show a trend that disagrees with expectations (*i.e.*, modulation is larger for protons in the **preMAX** phase, similar in the **MAX** phase, and larger for antiprotons in the **postMAX** phase), contrary to what is observed for the time-dependent fits, discussed in the main text. This seems to confirm that using a single modulation across different solar phases, especially if the solar maximum is included, introduces biases in the fit and produce unreliable results. The **HelMod** modulation instead uses a different modulation appropriate for each time period, and indeed the resulting time-dependent potential (bottom panel of Fig. B.1) is more in agreement with expectations, although not perfect, especially in the **postMAX** period. Regarding the PAMELA data, one can see an offset of the proton potential in the period in which the PAMELA and AMS-02 data overlap. This reflects a systematic offset originally present in the proton flux itself between the two datasets. There also exists a systematic offset in the two PAMELA antiproton datasets despite the fact that they cover almost the same time period.

The results for the **reacc** case, shown in Fig. B.2, show the same trend observed for the time-dependent fits, with a general disagreement with expectations indicating some issue with the related LIS. The **HelMod** case, instead, gives results very similar to the **conv** case. This is somehow expected, as the modulation model is fixed and thus seems to force the same LIS independently of the propagation model.

Appendix C: Propagation Model parameters and full fit results

The propagation model in our analysis is based on the propagation model developed in [52–54, 56], where we refer the reader to for full details. In short, the model comes in two variations: the convection model (**conv**) and the re-acceleration model (**reacc**), where the latter allows for re-acceleration of cosmic rays during propagation (see also Sec. III). Our free parameters include:

- Cosmic-ray injection spectra: in the **conv** case the injection spectra are pure powerlaws with spectral index $\gamma_{1,p}$ for protons, $\gamma_{1,He}$ for Helium and $\gamma_{1,CNO}$ for heavier primary nuclei. For the fit, in practice, the differences with respect to the proton spectral index are used, *i.e.*, $\gamma_{1,He-p}$ and $\gamma_{1,CNO-p}$. In the **reacc** model, we also include a break in the injection spectrum with a smoothing factor, R_{inj} and s_{inj} , respectively. Correspondingly, additional spectral indices below the break are given by $\gamma_{0,p}$, $\gamma_{0,He}$, $\gamma_{0,CNO}$.
- Diffusion: The diffusion coefficient is modelled as doubly broken power-law in the **conv** model, with normalization D_0 , breaks $R_{D,1}$ and $R_{D,2}$ and corresponding smoothing transition factors $s_{D,1}$ and $s_{D,2}$. The spectral indices at lower, intermediate

and higher rigidities are δ_l , δ and δ_h , respectively. In the **reacc** model the first diffusion break is not present, and is replaced instead by a break in the injection spectrum as mentioned above.

- The convection velocity $v_{0,c}$ in the **conv** model, and the Alfvén velocity v_A in the **reacc** model, respectively.
- The abundances of the primary nuclei, Abd_{12C} , Abd_{14N} and Abd_{16O} .
- Cross sections: The re-normalisation of the Helium-4 to Helium-3 cross section, together with a change of the slope, $A_{xs^4He \rightarrow ^3He}$ and $\delta_{xs^4He \rightarrow ^3He}$, respectively, and similarly for Carbon ($A_{xs \rightarrow C}$, $\delta_{xs \rightarrow C}$), Nitrogen ($A_{xs \rightarrow N}$, $\delta_{xs \rightarrow N}$), and Boron ($\delta_{xs \rightarrow B}$).
- Further normalization: The normalisation of the spectra for protons A_p , Helium A_{He} , the Boron-to-Carbon ratio A_B and the antiproton-to-proton ratio $A_{\bar{p}}$.
- Parameters related to the specific solar modulation model, see Section IV.

Tables C.1 to C.5 list all model parameters, priors, best-fit values and χ^2 values for each of our fits. The results are also reported in graphical form in Figures C.1 and C.2 for the **conv** and **reacc** models, respectively.

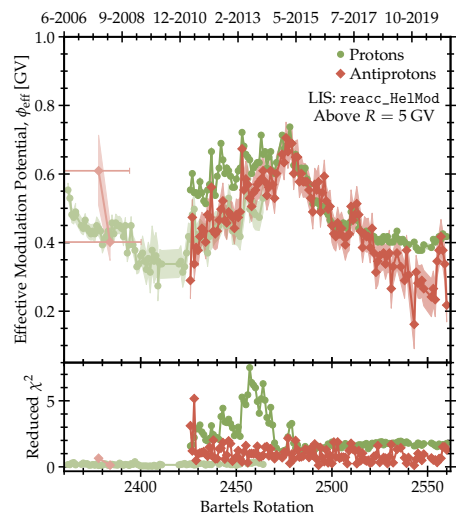
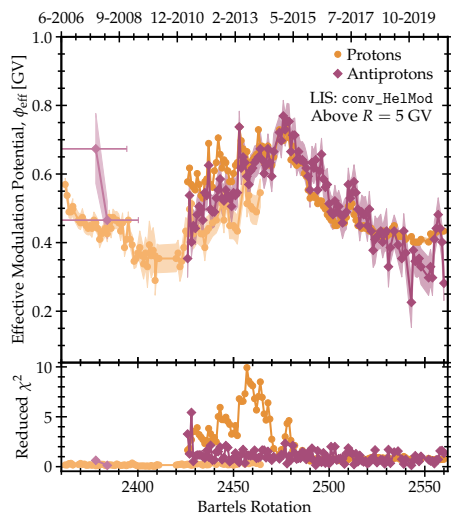
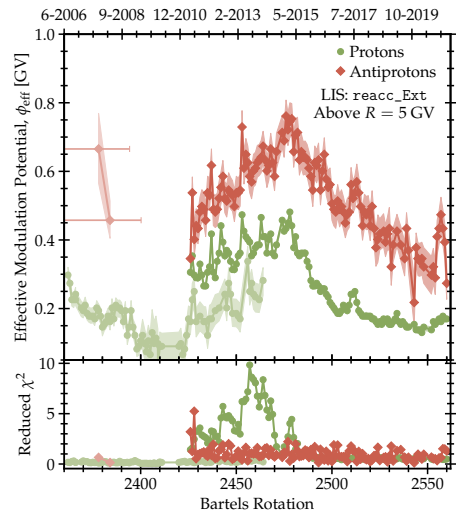
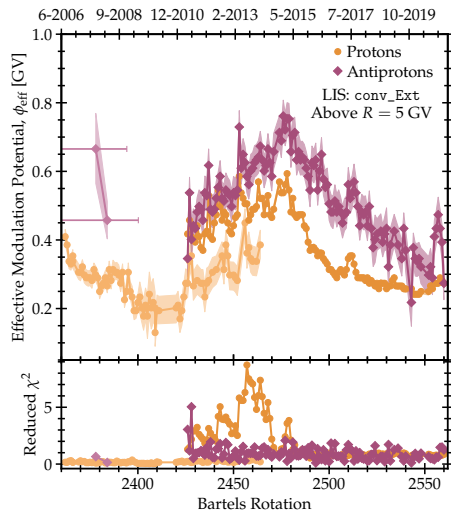
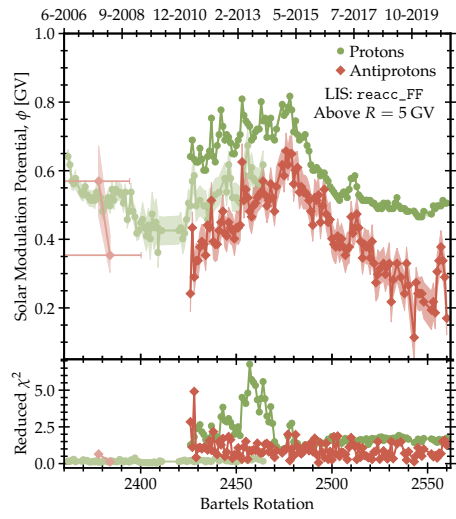
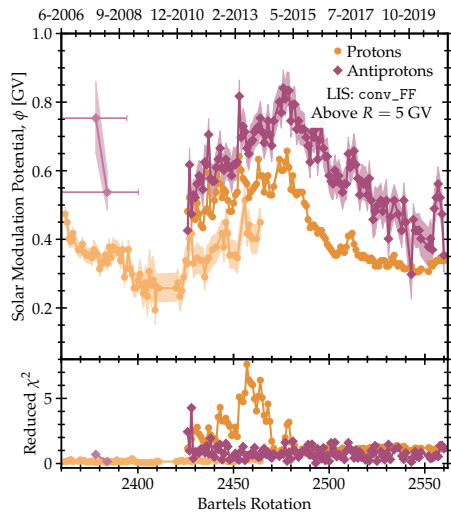


FIG. B.1: Effective force-field solar modulation potential for each Bartels rotation, for protons (orange circle markers) and antiprotons (burgundy diamond markers). Results are shown for the **conv** propagation model, where the top panel uses the force-field (FF) 7-yr AMS-02 fit LIS, middle panel the extended model (**Ext**) LIS and bottom panel the **He1Mod** LIS. Only rigidities above 5 GV are used to derive the potential. Lighter shades correspond to points fitted to the PAMELA data, while darker points correspond to fits to AMS-02 data.

FIG. B.2: Same as Fig. B.1 but for the **reacc** propagation model. Green circle markers correspond to protons and red diamond markers to antiprotons. Lighter shades represent the potentials based on PAMELA data.

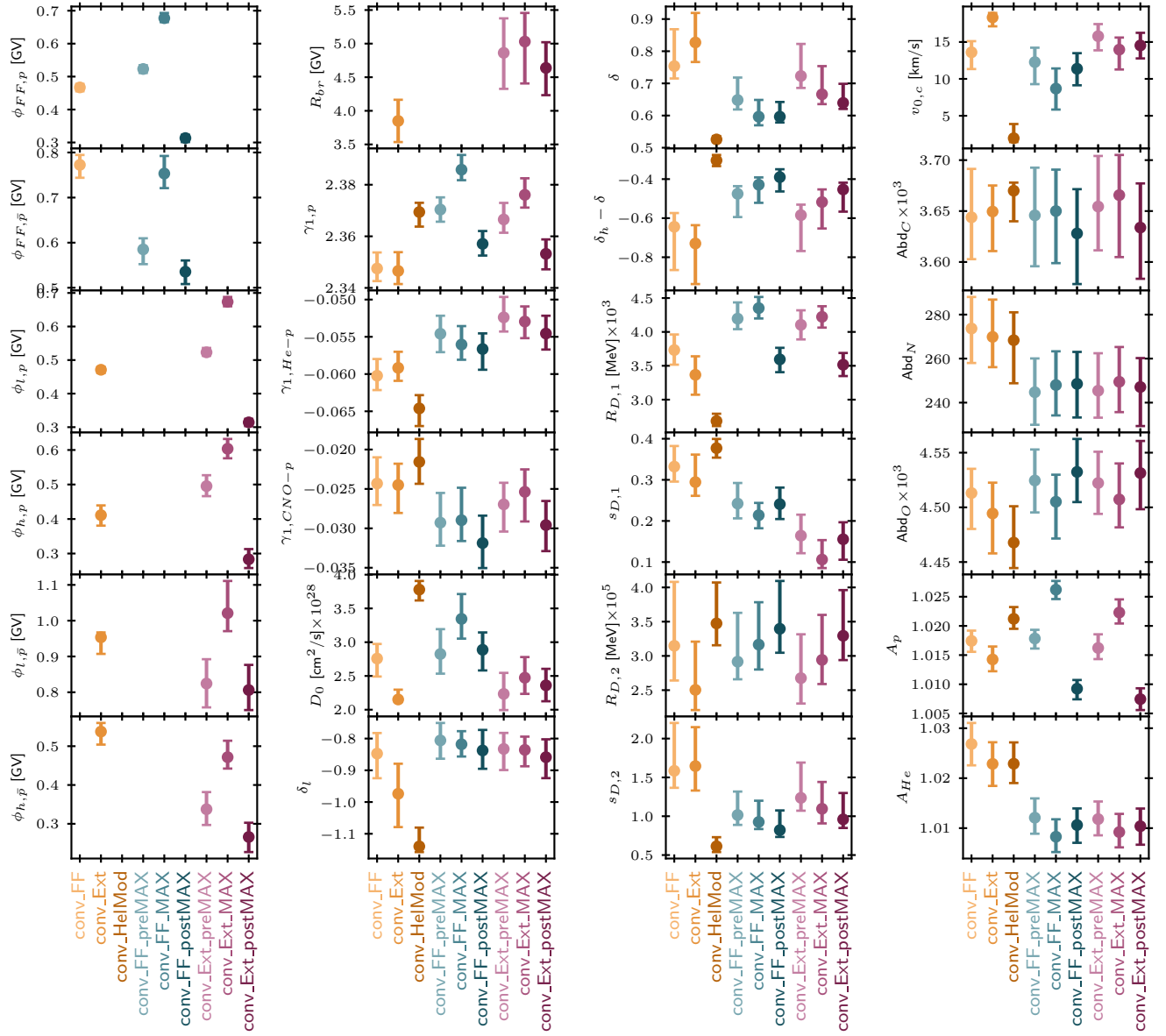


FIG. C.1: Best-fit values for the free parameters in the convection model, for the fits to the 7-yr AMS-02 data with solar modulation models for force-field (conv_FF), extended force-field (conv_Ext) and HelMod (conv_HelMod), as well as for the 3 time-dependent force-field fits (conv_FF_preMAX, conv_FF_MAX and conv_FF_postMAX, respectively), and the 3 time-dependent extended force-field fits (conv_Ext_preMAX, conv_Ext_MAX and conv_Ext_postMAX, respectively).

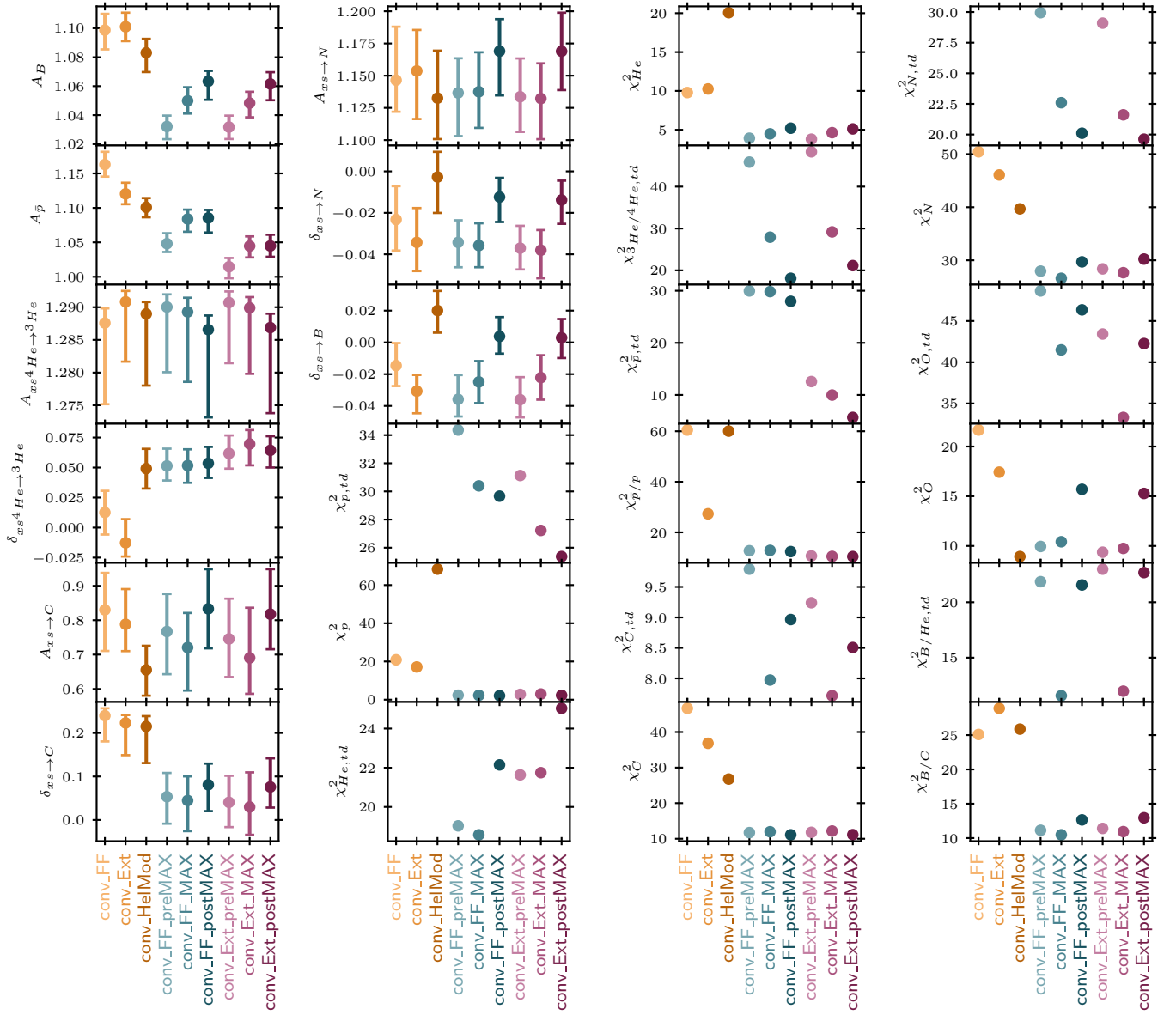


FIG. C.1 (cont.): Same as Fig. C.1. The χ^2 are given for AMS-02 data, where the subscript td indicates time-dependent data, unless otherwise indicated.

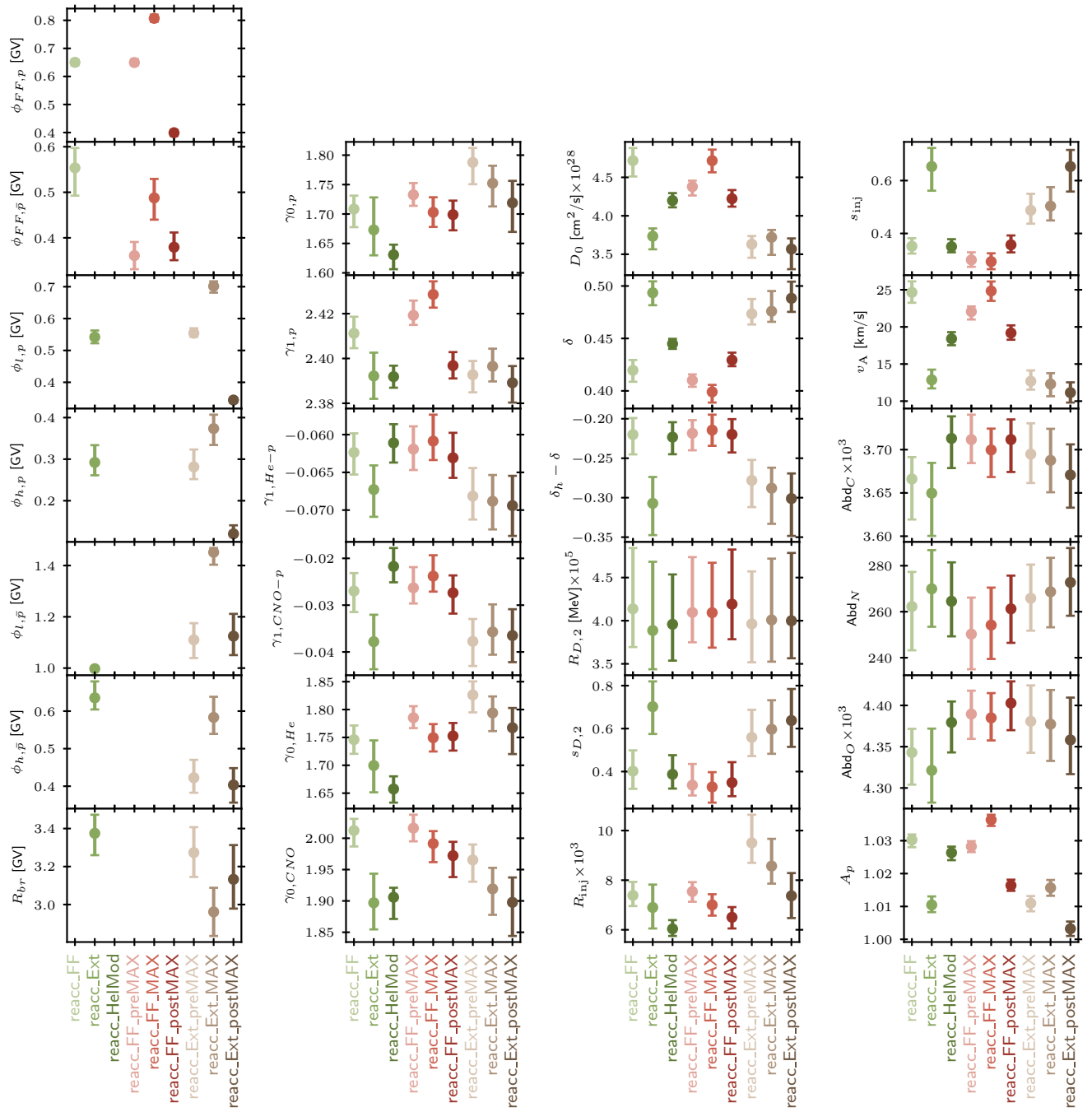


FIG. C.2: Best-fit values for the free parameters in the re-acceleration model, for the fits to the 7-yr AMS-02 data with solar modulation models for force-field (`reacc_FF`), extended force-field (`reacc_Ext`) and HelMod (`reacc_HelMod`), as well as for the 3 time-dependent force-field fits (`reacc_FF_preMAX`, `reacc_FF_MAX` and `reacc_FF_postMAX`, respectively), and the 3 time-dependent extended force-field fits (`reacc_Ext_preMAX`, `reacc_Ext_MAX` and `reacc_Ext_postMAX`, respectively).

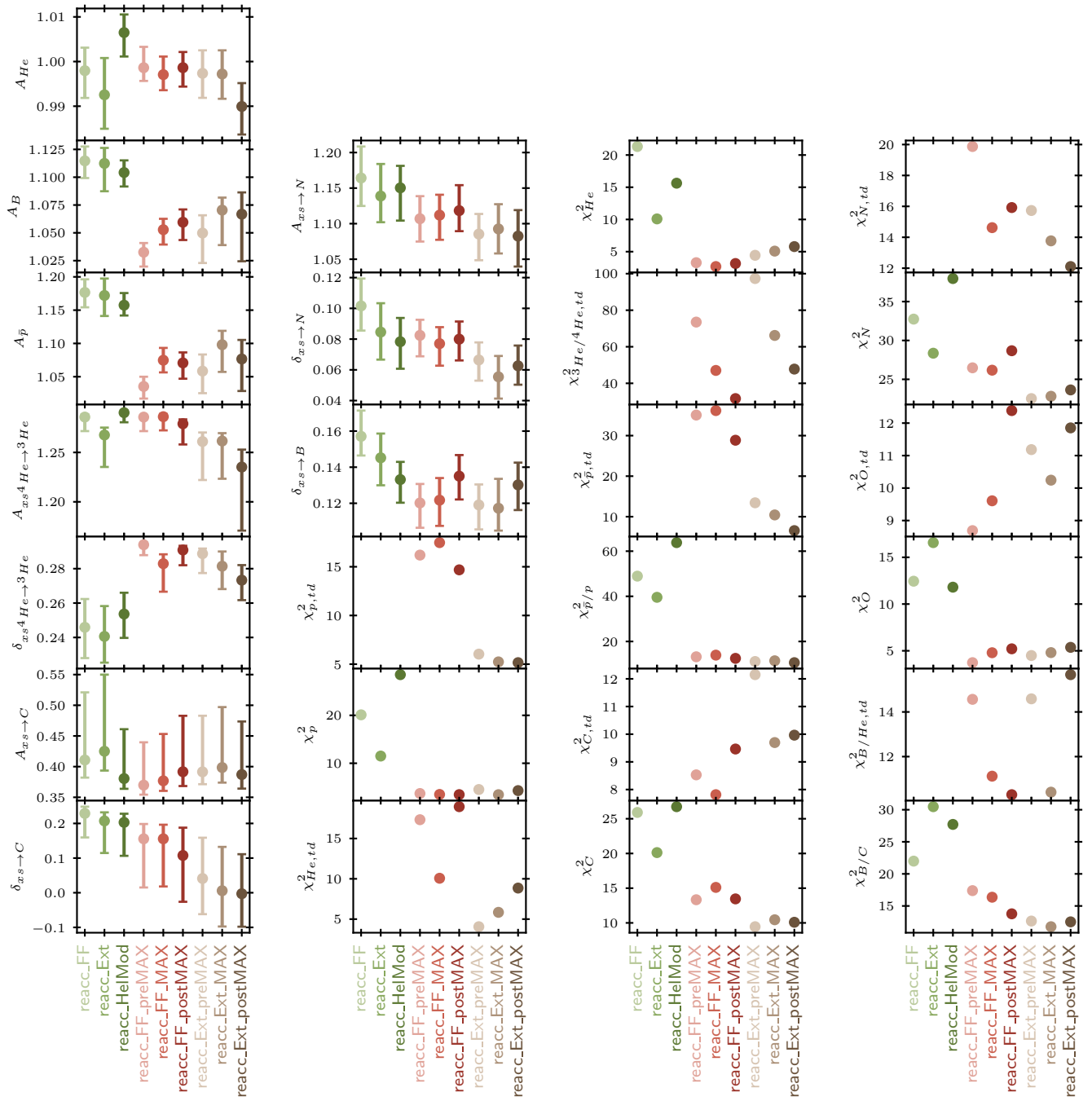


FIG. C.2 (cont.): Same as Fig. C.2. The χ^2 are given for AMS-02 data, where the subscript td indicates time-dependent data, unless otherwise indicated.

TABLE C.1: Summary of the best-fit parameters in the `conv` propagation model for the 3 time-dependent and the 7-yr time-integrated fit for the force-field solar modulation model (FF).

Parameter	Prior	<code>conv_FF_preMAX</code>	<code>conv_FF_MAX</code>	<code>conv_FF_postMAX</code>	<code>conv_FF</code>
$\phi_{FF,p}$ [GV]	0.1 – 1.0	$0.52^{+0.01}_{-0.01}$	$0.68^{+0.02}_{-0.01}$	$0.31^{+0.01}_{-0.01}$	$0.47^{+0.01}_{-0.01}$
$\phi_{FF,\bar{p}}$ [GV]	0.1 – 1.0	$0.59^{+0.02}_{-0.03}$	$0.75^{+0.04}_{-0.03}$	$0.54^{+0.02}_{-0.03}$	$0.77^{+0.02}_{-0.03}$
$\phi_{l,p}$ [GV]	–	–	–	–	–
$\phi_{h,p}$ [GV]	–	–	–	–	–
$\phi_{l,\bar{p}}$ [GV]	–	–	–	–	–
$\phi_{h,\bar{p}}$ [GV]	–	–	–	–	–
R_{br} [GV]	–	–	–	–	–
$\gamma_{1,p}$	2.3 – 2.42	$2.370^{+0.005}_{-0.005}$	$2.386^{+0.006}_{-0.004}$	$2.357^{+0.005}_{-0.005}$	$2.348^{+0.006}_{-0.005}$
$\gamma_{1,He-p}$	–0.09 – –0.03	$-0.055^{+0.002}_{-0.002}$	$-0.056^{+0.002}_{-0.002}$	$-0.057^{+0.002}_{-0.003}$	$-0.060^{+0.002}_{-0.002}$
$\gamma_{1,CNO-p}$	–0.05 – 0.0	$-0.029^{+0.004}_{-0.003}$	$-0.029^{+0.004}_{-0.003}$	$-0.032^{+0.003}_{-0.003}$	$-0.024^{+0.003}_{-0.003}$
D_0 [cm ² /s] $\times 10^{28}$	1 – 6	$2.8^{+0.4}_{-0.3}$	$3.3^{+0.4}_{-0.3}$	$2.9^{+0.3}_{-0.3}$	$2.8^{+0.2}_{-0.3}$
δ_l	–1.2 – –0.4	$-0.81^{+0.06}_{-0.06}$	$-0.82^{+0.04}_{-0.04}$	$-0.84^{+0.06}_{-0.06}$	$-0.85^{+0.06}_{-0.08}$
δ	0.3 – 1.0	$0.65^{+0.07}_{-0.03}$	$0.60^{+0.05}_{-0.03}$	$0.60^{+0.05}_{-0.02}$	$0.75^{+0.1}_{-0.04}$
$\delta_h - \delta$	–1.2 – –0.2	$-0.48^{+0.04}_{-0.1}$	$-0.43^{+0.04}_{-0.09}$	$-0.39^{+0.04}_{-0.07}$	$-0.64^{+0.07}_{-0.2}$
$R_{D,1}$ [MeV] $\times 10^3$	2.0 – 6	$4.2^{+0.2}_{-0.2}$	$4.4^{+0.2}_{-0.2}$	$3.6^{+0.2}_{-0.2}$	$3.7^{+0.2}_{-0.2}$
$s_{D,1}$	0.05 – 0.6	$0.24^{+0.05}_{-0.04}$	$0.21^{+0.03}_{-0.03}$	$0.24^{+0.04}_{-0.04}$	$0.33^{+0.05}_{-0.04}$
$R_{D,2}$ [MeV] $\times 10^5$	0.8 – 5	$2.9^{+0.7}_{-0.3}$	$3.2^{+0.6}_{-0.4}$	$3.4^{+0.7}_{-0.3}$	$3.1^{+0.9}_{-0.5}$
$s_{D,2}$	0.05 – 3.0	$1.0^{+0.3}_{-0.1}$	$0.93^{+0.3}_{-0.09}$	$0.82^{+0.3}_{-0.09}$	$1.6^{+0.6}_{-0.2}$
$v_{0,c}$ [km/s]	0.0 – 30	12^{+2}_{-3}	8^{+3}_{-3}	11^{+2}_{-2}	13^{+2}_{-2}
$Abd_C \times 10^3$	3.5 – 3.8	$3.65^{+0.05}_{-0.05}$	$3.65^{+0.04}_{-0.05}$	$3.63^{+0.04}_{-0.05}$	$3.64^{+0.05}_{-0.04}$
Abd_N	200 – 350	244^{+15}_{-15}	247^{+15}_{-14}	248^{+15}_{-15}	273^{+14}_{-16}
$Abd_O \times 10^3$	4.35 – 4.65	$4.52^{+0.03}_{-0.03}$	$4.51^{+0.02}_{-0.03}$	$4.53^{+0.03}_{-0.03}$	$4.51^{+0.02}_{-0.03}$
A_p	0.9 – 1.1	$1.018^{+0.001}_{-0.002}$	$1.026^{+0.001}_{-0.002}$	$1.009^{+0.001}_{-0.002}$	$1.017^{+0.002}_{-0.002}$
A_{He}	0.9 – 1.1	$1.012^{+0.004}_{-0.003}$	$1.008^{+0.003}_{-0.003}$	$1.011^{+0.003}_{-0.004}$	$1.027^{+0.004}_{-0.004}$
A_B	0.7 – 1.3	$1.032^{+0.008}_{-0.009}$	$1.050^{+0.009}_{-0.009}$	$1.063^{+0.007}_{-0.01}$	$1.10^{+0.01}_{-0.01}$
$A_{\bar{p}}$	0.7 – 1.3	$1.05^{+0.02}_{-0.01}$	$1.08^{+0.01}_{-0.02}$	$1.09^{+0.01}_{-0.02}$	$1.16^{+0.02}_{-0.02}$
$A_{xs^4He \rightarrow ^3He}$	0.7 – 1.3	$1.290^{+0.002}_{-0.01}$	$1.289^{+0.002}_{-0.01}$	$1.287^{+0.002}_{-0.01}$	$1.288^{+0.002}_{-0.01}$
$\delta_{xs^4He \rightarrow ^3He}$	–0.3 – 0.3	$0.05^{+0.01}_{-0.01}$	$0.05^{+0.01}_{-0.01}$	$0.05^{+0.01}_{-0.01}$	$0.01^{+0.02}_{-0.02}$
$A_{xs \rightarrow C}$	0.3 – 2.0	$0.8^{+0.1}_{-0.1}$	$0.7^{+0.1}_{-0.1}$	$0.8^{+0.1}_{-0.1}$	$0.8^{+0.1}_{-0.1}$
$\delta_{xs \rightarrow C}$	–0.3 – 0.3	$0.05^{+0.05}_{-0.06}$	$0.04^{+0.06}_{-0.07}$	$0.08^{+0.05}_{-0.06}$	$0.24^{+0.02}_{-0.06}$
$A_{xs \rightarrow N}$	0.7 – 1.3	$1.14^{+0.03}_{-0.03}$	$1.14^{+0.03}_{-0.03}$	$1.17^{+0.02}_{-0.03}$	$1.15^{+0.04}_{-0.02}$
$\delta_{xs \rightarrow N}$	–0.3 – 0.3	$-0.03^{+0.01}_{-0.01}$	$-0.04^{+0.01}_{-0.01}$	$-0.012^{+0.009}_{-0.01}$	$-0.02^{+0.02}_{-0.01}$
$\delta_{xs \rightarrow B}$	–0.3 – 0.3	$-0.04^{+0.02}_{-0.01}$	$-0.02^{+0.01}_{-0.01}$	$0.00^{+0.01}_{-0.01}$	$-0.01^{+0.01}_{-0.01}$

TABLE C.1 (cont.): Summary of the corresponding χ^2 values. Where two numbers are given for the datapoints, the first number indicates the number of datapoints in the time-dependent fit (where only datapoints above a certain rigidity are included, where solar modulation effects become negligible, see main text), and the second number the number of datapoints in the 7-yr time-integrated fit.

Parameter	# Datapoints	conv_FF_preMAX	conv_FF_MAX	conv_FF_postMAX	conv_FF
$\chi_{p,td}^2$	10	34.4	30.4	29.7	—
χ_p^2	27, 72	2.3	2.3	2.1	20.9
$\chi_{p,CALET}^2$	23	6.7	6.4	6.7	5.2
$\chi_{p,Voyager}^2$	6	9.1	13.8	7.9	5.5
$\chi_{He,td}^2$	40	19.0	18.6	22.1	—
χ_{He}^2	28, 68	3.9	4.5	5.2	9.8
$\chi_{He,DAMPE}^2$	21	7.1	6.8	6.9	6.5
$\chi_{He,Voyager}^2$	7	25.2	31.4	25.3	23.5
$\chi_{^3He/^4He,td}^2$	26	45.9	27.9	18.1	—
$\chi_{\bar{p},td}^2$	10	30.0	29.8	28.0	—
$\chi_{\bar{p}/p}^2$	18, 58	12.7	12.9	12.4	60.5
$\chi_{C,td}^2$	40	9.8	8.0	9.0	—
χ_C^2	28, 68	11.7	12.0	11.1	46.7
$\chi_{N,td}^2$	40	29.9	22.6	20.1	—
χ_N^2	27, 66	28.0	26.6	29.7	50.4
$\chi_{O,td}^2$	40	48.6	41.5	46.4	—
χ_O^2	28, 67	9.9	10.4	15.7	21.7
$\chi_{B/He,td}^2$	41, —	21.9	11.6	21.6	—
$\chi_{B/C}^2$	27, 67	11.1	10.5	12.6	25.1
$\chi_{B/C,DAMPE}^2$	13	14.7	10.9	19.2	28.8

TABLE C.2: Summary of the best-fit parameters in the conv propagation model for the 3 time-dependent and the 7-yr time-integrated fit for the extended solar modulation model (Ext).

Parameter	Prior	conv_Ext_preMAX	conv_Ext_MAX	conv_Ext_postMAX	conv_Ext
$\phi_{FF,p}$ [GV]	–	–	–	–	–
$\phi_{FF,\bar{p}}$ [GV]	–	–	–	–	–
$\phi_{l,p}$ [GV]	0.1 – 1.5	$0.52^{+0.01}_{-0.01}$	$0.67^{+0.01}_{-0.01}$	$0.31^{+0.01}_{-0.01}$	$0.471^{+0.009}_{-0.01}$
$\phi_{h,p}$ [GV]	0.1 – 1.5	$0.50^{+0.03}_{-0.03}$	$0.60^{+0.03}_{-0.03}$	$0.28^{+0.03}_{-0.03}$	$0.41^{+0.03}_{-0.03}$
$\phi_{l,\bar{p}}$ [GV]	0.1 – 1.5	$0.82^{+0.07}_{-0.07}$	$1.02^{+0.09}_{-0.05}$	$0.81^{+0.07}_{-0.06}$	$0.95^{+0.01}_{-0.05}$
$\phi_{h,\bar{p}}$ [GV]	0.1 – 1.5	$0.34^{+0.04}_{-0.04}$	$0.47^{+0.04}_{-0.03}$	$0.27^{+0.04}_{-0.04}$	$0.54^{+0.02}_{-0.03}$
R_{br} [GV]	1.0 – 6.0	$4.9^{+0.5}_{-0.5}$	$5.0^{+0.4}_{-0.6}$	$4.6^{+0.4}_{-0.4}$	$3.8^{+0.3}_{-0.3}$
$\gamma_{1,p}$	2.3 – 2.42	$2.367^{+0.006}_{-0.005}$	$2.376^{+0.006}_{-0.005}$	$2.353^{+0.006}_{-0.006}$	$2.347^{+0.007}_{-0.005}$
$\gamma_{1,He-p}$	–0.09 – –0.03	$-0.052^{+0.003}_{-0.002}$	$-0.053^{+0.002}_{-0.002}$	$-0.055^{+0.002}_{-0.002}$	$-0.059^{+0.002}_{-0.002}$
$\gamma_{1,CNO-p}$	–0.05 – 0.0	$-0.027^{+0.003}_{-0.003}$	$-0.025^{+0.003}_{-0.004}$	$-0.030^{+0.003}_{-0.003}$	$-0.025^{+0.003}_{-0.004}$
D_0 [cm ² /s] $\times 10^{28}$	1 – 6	$2.2^{+0.3}_{-0.2}$	$2.5^{+0.3}_{-0.2}$	$2.4^{+0.2}_{-0.2}$	$2.15^{+0.1}_{-0.04}$
δ_l	–1.2 – –0.4	$-0.83^{+0.05}_{-0.07}$	$-0.84^{+0.04}_{-0.05}$	$-0.86^{+0.06}_{-0.07}$	$-0.97^{+0.09}_{-0.1}$
δ	0.3 – 1.0	$0.72^{+0.1}_{-0.04}$	$0.67^{+0.09}_{-0.03}$	$0.64^{+0.06}_{-0.02}$	$0.83^{+0.09}_{-0.06}$
$\delta_h - \delta$	–1.2 – –0.2	$-0.58^{+0.05}_{-0.2}$	$-0.52^{+0.06}_{-0.1}$	$-0.45^{+0.03}_{-0.1}$	$-0.73^{+0.09}_{-0.2}$
$R_{D,1}$ [MeV] $\times 10^3$	2.0 – 6	$4.1^{+0.2}_{-0.2}$	$4.2^{+0.2}_{-0.2}$	$3.5^{+0.2}_{-0.2}$	$3.4^{+0.3}_{-0.3}$
$s_{D,1}$	0.05 – 0.6	$0.16^{+0.05}_{-0.04}$	$0.11^{+0.05}_{-0.02}$	$0.16^{+0.04}_{-0.05}$	$0.29^{+0.07}_{-0.03}$
$R_{D,2}$ [MeV] $\times 10^5$	0.8 – 5	$2.7^{+0.6}_{-0.4}$	$2.9^{+0.7}_{-0.4}$	$3.3^{+0.7}_{-0.4}$	$2.5^{+0.7}_{-0.3}$
$s_{D,2}$	0.05 – 3.0	$1.2^{+0.5}_{-0.2}$	$1.1^{+0.3}_{-0.2}$	$1.0^{+0.3}_{-0.1}$	$1.6^{+0.5}_{-0.3}$
$v_{0,c}$ [km/s]	0.0 – 30	15^{+2}_{-2}	13^{+2}_{-3}	14^{+2}_{-2}	18^{+1}_{-1}
$Abd_C \times 10^3$	3.5 – 3.8	$3.65^{+0.05}_{-0.04}$	$3.67^{+0.04}_{-0.06}$	$3.63^{+0.04}_{-0.05}$	$3.65^{+0.03}_{-0.04}$
Abd_N	200 – 350	245^{+17}_{-12}	249^{+16}_{-14}	247^{+13}_{-18}	269^{+17}_{-14}
$Abd_O \times 10^3$	4.35 – 4.65	$4.52^{+0.03}_{-0.03}$	$4.51^{+0.03}_{-0.03}$	$4.53^{+0.03}_{-0.03}$	$4.49^{+0.03}_{-0.04}$
A_p	0.9 – 1.1	$1.016^{+0.002}_{-0.002}$	$1.022^{+0.002}_{-0.002}$	$1.007^{+0.002}_{-0.002}$	$1.014^{+0.002}_{-0.002}$
A_{He}	0.9 – 1.1	$1.012^{+0.004}_{-0.003}$	$1.009^{+0.004}_{-0.003}$	$1.010^{+0.004}_{-0.004}$	$1.023^{+0.004}_{-0.004}$
A_B	0.7 – 1.3	$1.032^{+0.008}_{-0.008}$	$1.048^{+0.008}_{-0.01}$	$1.062^{+0.008}_{-0.01}$	$1.10^{+0.01}_{-0.01}$
$A_{\bar{p}}$	0.7 – 1.3	$1.01^{+0.01}_{-0.02}$	$1.04^{+0.01}_{-0.02}$	$1.04^{+0.02}_{-0.02}$	$1.12^{+0.02}_{-0.02}$
$A_{xs^4He \rightarrow ^3He}$	0.7 – 1.3	$1.291^{+0.002}_{-0.009}$	$1.290^{+0.002}_{-0.01}$	$1.287^{+0.002}_{-0.01}$	$1.291^{+0.002}_{-0.009}$
$\delta_{xs^4He \rightarrow ^3He}$	–0.3 – 0.3	$0.06^{+0.01}_{-0.01}$	$0.07^{+0.01}_{-0.02}$	$0.06^{+0.01}_{-0.01}$	$-0.01^{+0.02}_{-0.01}$
$A_{xs \rightarrow C}$	0.3 – 2.0	$0.7^{+0.1}_{-0.1}$	$0.7^{+0.1}_{-0.1}$	$0.8^{+0.1}_{-0.1}$	$0.79^{+0.1}_{-0.08}$
$\delta_{xs \rightarrow C}$	–0.3 – 0.3	$0.04^{+0.06}_{-0.06}$	$0.03^{+0.08}_{-0.06}$	$0.08^{+0.07}_{-0.05}$	$0.22^{+0.02}_{-0.07}$
$A_{xs \rightarrow N}$	0.7 – 1.3	$1.13^{+0.03}_{-0.03}$	$1.13^{+0.03}_{-0.03}$	$1.17^{+0.03}_{-0.03}$	$1.15^{+0.03}_{-0.04}$
$\delta_{xs \rightarrow N}$	–0.3 – 0.3	$-0.04^{+0.01}_{-0.01}$	$-0.04^{+0.01}_{-0.01}$	$-0.014^{+0.009}_{-0.01}$	$-0.03^{+0.02}_{-0.01}$
$\delta_{xs \rightarrow B}$	–0.3 – 0.3	$-0.04^{+0.01}_{-0.01}$	$-0.02^{+0.01}_{-0.01}$	$0.00^{+0.01}_{-0.01}$	$-0.03^{+0.01}_{-0.01}$

TABLE C.2 (cont.): Summary of the corresponding χ^2 values.

Parameter	# Datapoints	conv_Ext_preMAX	conv_Ext_MAX	conv_Ext_postMAX	conv_Ext
$\chi_{p,td}^2$	10	31.1	27.2	25.4	–
χ_p^2	27, 72	2.8	3.0	2.3	17.1
$\chi_{p,CALET}^2$	23	8.0	7.9	8.1	6.8
$\chi_{p,Voyager}^2$	6	7.6	10.8	6.6	4.5
$\chi_{He,td}^2$	40	21.6	21.7	25.0	–
χ_{He}^2	28, 68	3.8	4.6	5.1	10.3
$\chi_{He,DAMPE}^2$	21	6.8	6.6	6.7	6.7
$\chi_{He,Voyager}^2$	7	22.8	26.2	22.1	21.5
$\chi_{He^3/He^4,td}^2$	26	48.3	29.2	21.1	–
$\chi_{\bar{p},td}^2$	10	12.6	10.0	5.7	–
$\chi_{\bar{p}/p}^2$	18, 58	10.7	10.5	10.4	27.3
$\chi_{C,td}^2$	40	9.2	7.7	8.5	–
χ_C^2	28, 68	11.8	12.2	11.1	36.8
$\chi_{N,td}^2$	40	29.1	21.6	19.6	–
χ_N^2	27, 66	28.4	27.7	30.2	46.1
$\chi_{O,td}^2$	40	43.4	33.3	42.3	–
χ_O^2	28, 67	9.4	9.7	15.3	17.4
$\chi_{B/He,td}^2$	41, –	23.0	12.0	22.7	–
$\chi_{B/C}^2$	27, 67	11.4	10.9	13.0	28.9
$\chi_{B/C,DAMPE}^2$	13	15.5	13.1	19.8	27.4

TABLE C.3: Summary of the best-fit parameters in the **reacc** propagation model for the 3 time-dependent and the time-independent fit for the force-field solar modulation model (FF).

Parameter	Prior	reacc_FF_preMAX	reacc_FF_MAX	reacc_FF_postMAX	reacc_FF
$\phi_{FF,p}$ [GV]	0.1 – 1.0	$0.65^{+0.01}_{-0.01}$	$0.81^{+0.01}_{-0.01}$	$0.40^{+0.01}_{-0.01}$	$0.65^{+0.01}_{-0.01}$
$\phi_{FF,\bar{p}}$ [GV]	0.1 – 1.0	$0.36^{+0.03}_{-0.03}$	$0.49^{+0.04}_{-0.05}$	$0.38^{+0.03}_{-0.03}$	$0.55^{+0.04}_{-0.06}$
$\phi_{l,p}$ [GV]	–	–	–	–	–
$\phi_{h,p}$ [GV]	–	–	–	–	–
$\phi_{l,\bar{p}}$ [GV]	–	–	–	–	–
$\phi_{h,\bar{p}}$ [GV]	–	–	–	–	–
R_{br} [GV]	–	–	–	–	–
$\gamma_{0,p}$	1.5 – 2.0	$1.73^{+0.02}_{-0.02}$	$1.70^{+0.03}_{-0.02}$	$1.70^{+0.02}_{-0.03}$	$1.71^{+0.02}_{-0.03}$
$\gamma_{1,p}$	2.3 – 2.45	$2.419^{+0.007}_{-0.004}$	$2.429^{+0.006}_{-0.006}$	$2.397^{+0.006}_{-0.006}$	$2.411^{+0.007}_{-0.007}$
$\gamma_{1,He-p}$	–0.09 – –0.03	$-0.062^{+0.003}_{-0.003}$	$-0.061^{+0.004}_{-0.003}$	$-0.063^{+0.003}_{-0.003}$	$-0.062^{+0.003}_{-0.003}$
$\gamma_{1,CNO-p}$	–0.05 – 0.0	$-0.026^{+0.004}_{-0.003}$	$-0.024^{+0.004}_{-0.003}$	$-0.027^{+0.004}_{-0.004}$	$-0.027^{+0.004}_{-0.004}$
$\gamma_{0,He}$	1.5 – 2.0	$1.79^{+0.02}_{-0.02}$	$1.75^{+0.02}_{-0.02}$	$1.75^{+0.02}_{-0.03}$	$1.75^{+0.03}_{-0.03}$
$\gamma_{0,CNO}$	1.8 – 2.2	$2.02^{+0.02}_{-0.02}$	$1.99^{+0.02}_{-0.03}$	$1.97^{+0.02}_{-0.03}$	$2.01^{+0.02}_{-0.03}$
D_0 [cm ² /s] $\times 10^{28}$	1 – 8	$4.38^{+0.08}_{-0.1}$	$4.7^{+0.1}_{-0.2}$	$4.2^{+0.1}_{-0.1}$	$4.7^{+0.2}_{-0.2}$
δ	0.2 – 0.8	$0.410^{+0.006}_{-0.006}$	$0.399^{+0.007}_{-0.01}$	$0.429^{+0.007}_{-0.006}$	$0.42^{+0.01}_{-0.01}$
$\delta_h - \delta$	–1.0 – –0.1	$-0.22^{+0.02}_{-0.02}$	$-0.21^{+0.02}_{-0.02}$	$-0.22^{+0.02}_{-0.02}$	$-0.22^{+0.02}_{-0.03}$
$R_{D,2}$ [MeV] $\times 10^5$	1 – 7	$4.1^{+0.6}_{-0.3}$	$4.1^{+0.6}_{-0.4}$	$4.2^{+0.6}_{-0.4}$	$4.1^{+0.7}_{-0.4}$
$s_{D,2}$	0.05 – 1.0	$0.34^{+0.1}_{-0.05}$	$0.33^{+0.07}_{-0.07}$	$0.35^{+0.1}_{-0.06}$	$0.40^{+0.1}_{-0.08}$
$R_{inj} \times 10^3$	3 – 15	$7.5^{+0.4}_{-0.4}$	$7.0^{+0.4}_{-0.4}$	$6.5^{+0.4}_{-0.5}$	$7.4^{+0.5}_{-0.4}$
s_{inj}	0.05 – 0.8	$0.30^{+0.03}_{-0.03}$	$0.29^{+0.03}_{-0.03}$	$0.36^{+0.04}_{-0.03}$	$0.35^{+0.03}_{-0.03}$
v_A [km/s]	0.0 – 35	22^{+1}_{-1}	24^{+1}_{-1}	19^{+1}_{-1}	24^{+1}_{-1}
$Abd_C \times 10^3$	3.5 – 3.8	$3.71^{+0.03}_{-0.03}$	$3.70^{+0.02}_{-0.03}$	$3.71^{+0.02}_{-0.04}$	$3.67^{+0.03}_{-0.05}$
Abd_N	200 – 350	250^{+16}_{-15}	254^{+16}_{-15}	261^{+14}_{-15}	262^{+15}_{-19}
$Abd_O \times 10^3$	4.0 – 4.65	$4.39^{+0.03}_{-0.03}$	$4.38^{+0.03}_{-0.03}$	$4.40^{+0.03}_{-0.03}$	$4.34^{+0.03}_{-0.04}$
A_p	0.9 – 1.1	$1.028^{+0.002}_{-0.002}$	$1.036^{+0.002}_{-0.002}$	$1.016^{+0.002}_{-0.002}$	$1.030^{+0.002}_{-0.002}$
A_{He}	0.9 – 1.1	$0.999^{+0.005}_{-0.003}$	$0.997^{+0.004}_{-0.003}$	$0.999^{+0.004}_{-0.004}$	$0.998^{+0.005}_{-0.006}$
A_B	0.7 – 1.3	$1.033^{+0.008}_{-0.01}$	$1.05^{+0.01}_{-0.01}$	$1.06^{+0.01}_{-0.02}$	$1.11^{+0.01}_{-0.02}$
$A_{\bar{p}}$	0.7 – 1.3	$1.04^{+0.01}_{-0.02}$	$1.07^{+0.02}_{-0.02}$	$1.07^{+0.02}_{-0.02}$	$1.18^{+0.02}_{-0.02}$
$A_{xs^4He \rightarrow ^3He}$	0.7 – 1.3	$1.286^{+0.002}_{-0.01}$	$1.286^{+0.003}_{-0.01}$	$1.279^{+0.004}_{-0.02}$	$1.286^{+0.003}_{-0.01}$
$\delta_{xs^4He \rightarrow ^3He}$	–0.3 – 0.3	$0.294^{+0.001}_{-0.006}$	$0.283^{+0.005}_{-0.02}$	$0.291^{+0.002}_{-0.009}$	$0.25^{+0.02}_{-0.02}$
$A_{xs \rightarrow C}$	0.3 – 2.0	$0.37^{+0.07}_{-0.02}$	$0.38^{+0.08}_{-0.02}$	$0.39^{+0.09}_{-0.02}$	$0.41^{+0.1}_{-0.03}$
$\delta_{xs \rightarrow C}$	–0.3 – 0.3	$0.16^{+0.04}_{-0.1}$	$0.16^{+0.04}_{-0.1}$	$0.11^{+0.08}_{-0.1}$	$0.23^{+0.02}_{-0.07}$
$A_{xs \rightarrow N}$	0.7 – 1.3	$1.11^{+0.03}_{-0.03}$	$1.11^{+0.03}_{-0.03}$	$1.12^{+0.04}_{-0.03}$	$1.16^{+0.04}_{-0.04}$
$\delta_{xs \rightarrow N}$	–0.3 – 0.3	$0.08^{+0.01}_{-0.01}$	$0.08^{+0.01}_{-0.01}$	$0.08^{+0.01}_{-0.01}$	$0.10^{+0.02}_{-0.02}$
$\delta_{xs \rightarrow B}$	–0.3 – 0.3	$0.12^{+0.01}_{-0.01}$	$0.12^{+0.01}_{-0.01}$	$0.14^{+0.01}_{-0.01}$	$0.16^{+0.01}_{-0.01}$

TABLE C.3 (cont.): Summary of the corresponding χ^2 values.

Parameter	# Datapoints	reacc_FF_preMAX	reacc_FF_MAX	reacc_FF_postMAX	reacc_FF
$\chi_{p,td}^2$	10	16.2	17.5	14.7	–
χ_p^2	27, 72	3.7	3.5	3.5	20.1
$\chi_{p,CALET}^2$	23	5.6	6.0	5.8	5.8
$\chi_{p,Voyager}^2$	6	31.4	37.3	24.2	32.3
$\chi_{He,td}^2$	40	17.3	10.1	18.9	–
χ_{He}^2	28, 68	3.3	2.7	3.2	21.3
$\chi_{He,DAMPE}^2$	21	8.4	8.1	7.9	7.7
$\chi_{He,Voyager}^2$	7	26.4	34.5	20.8	29.8
$\chi_{He/4He,td}^2$	26	73.5	47.1	31.6	–
$\chi_{\bar{p},td}^2$	10	35.1	36.2	28.9	–
$\chi_{\bar{p}/p}^2$	18, 58	13.2	13.9	12.5	48.9
$\chi_{C,td}^2$	40	8.5	7.8	9.5	–
χ_C^2	28, 68	13.3	15.1	13.5	25.9
$\chi_{N,td}^2$	40	19.9	14.6	15.9	–
χ_N^2	27, 66	26.5	26.2	28.7	32.7
$\chi_{O,td}^2$	40	8.7	9.6	12.4	–
χ_O^2	28, 67	3.7	4.8	5.2	12.4
$\chi_{B/He,td}^2$	41, –	14.6	11.1	10.3	–
$\chi_{B/C}^2$	27, 67	17.4	16.4	13.8	22.0
$\chi_{B/C,DAMPE}^2$	13	3.6	2.7	7.9	6.7

TABLE C.4: Summary of the best-fit parameters in the `reacc` propagation model for the 3 time-dependent and the 7-yr time-integrated fit for the extended solar modulation model (Ext).

Parameter	Prior	reacc.Ext_preMAX	reacc.Ext_MAX	reacc.Ext_postMAX	reacc.Ext
$\phi_{FF,p}$ [GV]	–	–	–	–	–
$\phi_{FF,\bar{p}}$ [GV]	–	–	–	–	–
$\phi_{l,p}$ [GV]	0.1 – 1.5	$0.55^{+0.02}_{-0.01}$	$0.70^{+0.02}_{-0.02}$	$0.344^{+0.007}_{-0.008}$	$0.54^{+0.02}_{-0.02}$
$\phi_{h,p}$ [GV]	0.1 – 1.5	$0.28^{+0.04}_{-0.03}$	$0.37^{+0.03}_{-0.04}$	$0.120^{+0.02}_{-0.005}$	$0.29^{+0.04}_{-0.03}$
$\phi_{l,\bar{p}}$ [GV]	0.1 – 1.5	$1.11^{+0.06}_{-0.07}$	$1.45^{+0.02}_{-0.05}$	$1.12^{+0.09}_{-0.07}$	$0.998^{+0.002}_{-0.002}$
$\phi_{h,\bar{p}}$ [GV]	0.1 – 1.5	$0.42^{+0.05}_{-0.04}$	$0.58^{+0.05}_{-0.04}$	$0.40^{+0.04}_{-0.05}$	$0.64^{+0.04}_{-0.03}$
R_{br} [GV]	1.0 – 6.0	$3.3^{+0.1}_{-0.1}$	$3.0^{+0.1}_{-0.1}$	$3.1^{+0.2}_{-0.2}$	$3.4^{+0.1}_{-0.1}$
$\gamma_{0,p}$	1.5 – 2.0	$1.79^{+0.02}_{-0.04}$	$1.75^{+0.03}_{-0.04}$	$1.72^{+0.04}_{-0.05}$	$1.67^{+0.06}_{-0.04}$
$\gamma_{1,p}$	2.3 – 2.45	$2.393^{+0.006}_{-0.008}$	$2.396^{+0.008}_{-0.007}$	$2.389^{+0.007}_{-0.009}$	$2.39^{+0.01}_{-0.01}$
$\gamma_{1,He-p}$	–0.09 – –0.03	$-0.068^{+0.004}_{-0.003}$	$-0.069^{+0.003}_{-0.004}$	$-0.069^{+0.004}_{-0.004}$	$-0.067^{+0.003}_{-0.004}$
$\gamma_{1,CNO-p}$	–0.05 – 0.0	$-0.038^{+0.005}_{-0.005}$	$-0.036^{+0.006}_{-0.005}$	$-0.036^{+0.006}_{-0.006}$	$-0.038^{+0.006}_{-0.006}$
$\gamma_{0,He}$	1.5 – 2.0	$1.83^{+0.02}_{-0.03}$	$1.79^{+0.03}_{-0.03}$	$1.77^{+0.04}_{-0.05}$	$1.70^{+0.05}_{-0.05}$
$\gamma_{0,CNO}$	1.8 – 2.2	$1.97^{+0.02}_{-0.03}$	$1.92^{+0.03}_{-0.04}$	$1.90^{+0.04}_{-0.05}$	$1.90^{+0.05}_{-0.04}$
D_0 [cm ² /s] $\times 10^{28}$	1 – 8	$3.6^{+0.1}_{-0.2}$	$3.7^{+0.1}_{-0.2}$	$3.6^{+0.1}_{-0.3}$	$3.7^{+0.1}_{-0.2}$
δ	0.2 – 0.8	$0.47^{+0.01}_{-0.01}$	$0.48^{+0.02}_{-0.01}$	$0.49^{+0.02}_{-0.01}$	$0.49^{+0.01}_{-0.01}$
$\delta_h - \delta$	–1.0 – –0.1	$-0.28^{+0.03}_{-0.03}$	$-0.29^{+0.03}_{-0.05}$	$-0.30^{+0.03}_{-0.05}$	$-0.31^{+0.03}_{-0.04}$
$R_{D,2}$ [MeV] $\times 10^5$	1 – 7	$4.0^{+0.6}_{-0.4}$	$4.0^{+0.7}_{-0.5}$	$4.0^{+0.8}_{-0.4}$	$3.9^{+0.8}_{-0.4}$
$s_{D,2}$	0.05 – 1.0	$0.56^{+0.1}_{-0.09}$	$0.6^{+0.1}_{-0.1}$	$0.6^{+0.1}_{-0.1}$	$0.7^{+0.1}_{-0.1}$
$R_{inj} \times 10^3$	3 – 15	9^{+1}_{-1}	8^{+1}_{-1}	$7.4^{+0.9}_{-0.9}$	$6.9^{+0.9}_{-0.8}$
s_{inj}	0.05 – 0.8	$0.49^{+0.06}_{-0.05}$	$0.50^{+0.07}_{-0.05}$	$0.65^{+0.06}_{-0.09}$	$0.65^{+0.07}_{-0.09}$
v_A [km/s]	0.0 – 35	12^{+1}_{-1}	12^{+1}_{-2}	11^{+1}_{-1}	12^{+1}_{-1}
$Abd_C \times 10^3$	3.5 – 3.8	$3.69^{+0.04}_{-0.03}$	$3.69^{+0.04}_{-0.04}$	$3.67^{+0.04}_{-0.04}$	$3.65^{+0.04}_{-0.05}$
Abd_N	200 – 350	265^{+15}_{-14}	268^{+15}_{-15}	272^{+15}_{-15}	269^{+17}_{-16}
$Abd_O \times 10^3$	4.0 – 4.65	$4.38^{+0.04}_{-0.04}$	$4.38^{+0.04}_{-0.04}$	$4.36^{+0.05}_{-0.04}$	$4.32^{+0.05}_{-0.04}$
A_p	0.9 – 1.1	$1.011^{+0.002}_{-0.002}$	$1.016^{+0.002}_{-0.002}$	$1.003^{+0.002}_{-0.002}$	$1.010^{+0.003}_{-0.002}$
A_{He}	0.9 – 1.1	$0.997^{+0.005}_{-0.005}$	$0.997^{+0.005}_{-0.006}$	$0.990^{+0.005}_{-0.006}$	$0.993^{+0.008}_{-0.008}$
A_B	0.7 – 1.3	$1.05^{+0.02}_{-0.03}$	$1.07^{+0.01}_{-0.03}$	$1.07^{+0.02}_{-0.04}$	$1.11^{+0.01}_{-0.03}$
$A_{\bar{p}}$	0.7 – 1.3	$1.06^{+0.02}_{-0.03}$	$1.10^{+0.02}_{-0.04}$	$1.08^{+0.03}_{-0.05}$	$1.17^{+0.03}_{-0.03}$
$A_{xs^4He \rightarrow ^3He}$	0.7 – 1.3	$1.261^{+0.009}_{-0.04}$	$1.262^{+0.008}_{-0.04}$	$1.24^{+0.02}_{-0.06}$	$1.268^{+0.007}_{-0.03}$
$\delta_{xs^4He \rightarrow ^3He}$	–0.3 – 0.3	$0.289^{+0.003}_{-0.01}$	$0.281^{+0.009}_{-0.01}$	$0.273^{+0.009}_{-0.01}$	$0.24^{+0.02}_{-0.02}$
$A_{xs \rightarrow C}$	0.3 – 2.0	$0.39^{+0.09}_{-0.02}$	$0.40^{+0.1}_{-0.02}$	$0.39^{+0.09}_{-0.02}$	$0.43^{+0.1}_{-0.03}$
$\delta_{xs \rightarrow C}$	–0.3 – 0.3	$0.0^{+0.1}_{-0.1}$	$0.0^{+0.1}_{-0.1}$	$-0.0^{+0.1}_{-0.1}$	$0.21^{+0.02}_{-0.09}$
$A_{xs \rightarrow N}$	0.7 – 1.3	$1.09^{+0.03}_{-0.04}$	$1.09^{+0.03}_{-0.03}$	$1.08^{+0.04}_{-0.04}$	$1.14^{+0.05}_{-0.04}$
$\delta_{xs \rightarrow N}$	–0.3 – 0.3	$0.07^{+0.01}_{-0.01}$	$0.06^{+0.01}_{-0.01}$	$0.06^{+0.01}_{-0.01}$	$0.08^{+0.02}_{-0.02}$
$\delta_{xs \rightarrow B}$	–0.3 – 0.3	$0.12^{+0.01}_{-0.01}$	$0.12^{+0.02}_{-0.01}$	$0.13^{+0.01}_{-0.01}$	$0.15^{+0.01}_{-0.02}$

TABLE C.4 (cont.): Summary of the corresponding χ^2 values.

Parameter	# Datapoints	reacc_Ext_preMAX	reacc_Ext_MAX	reacc_Ext_postMAX	reacc_Ext
$\chi_{p,td}^2$	10	6.0	5.2	5.2	–
χ_p^2	27, 72	4.5	3.4	4.3	11.5
$\chi_{p,CALET}^2$	23	4.7	4.7	4.7	4.8
$\chi_{p,Voyager}^2$	6	9.4	9.2	9.3	11.5
$\chi_{He,td}^2$	40	4.1	5.8	8.9	–
χ_{He}^2	28, 68	4.4	5.1	5.8	10.1
$\chi_{He,DAMPE}^2$	21	7.8	7.4	7.5	7.0
$\chi_{He,Voyager}^2$	7	3.1	3.7	3.1	5.3
χ_{He^3/He^4}^2	26	97.3	66.2	47.8	–
$\chi_{\bar{p},td}^2$	10	13.4	10.4	6.6	–
$\chi_{\bar{p}/p}^2$	18, 58	11.1	11.4	10.6	39.6
$\chi_{C,td}^2$	40	12.2	9.7	10.0	–
χ_C^2	28, 68	9.4	10.4	10.1	20.1
$\chi_{N,td}^2$	40	15.7	13.8	12.1	–
χ_N^2	27, 66	22.5	22.8	23.6	28.4
$\chi_{O,td}^2$	40	11.2	10.2	11.9	–
χ_O^2	28, 67	4.5	4.8	5.4	16.6
$\chi_{B/He,td}^2$	41, –	14.6	10.4	15.7	–
$\chi_{B/C}^2$	27, 67	12.6	11.8	12.5	30.5
$\chi_{B/C,DAMPE}^2$	13	9.5	9.2	11.0	11.9

TABLE C.5: Summary of the best-fit parameters in the `conv` and `reacc` propagation models for the 7-yr time-integrated He1Mod solar modulation fits.

Parameter	Prior	<code>conv_He1Mod</code>	<code>reacc_He1Mod</code>
$\gamma_{0,p}$	1.5 – 2.0	$2.369^{+0.004}_{-0.006}$	$1.63^{+0.02}_{-0.02}$
$\gamma_{1,p}$	2.3 – 2.4	$2.369^{+0.004}_{-0.006}$	$2.392^{+0.005}_{-0.005}$
$\gamma_{1,He-p}$	-0.09 – -0.03	$-0.065^{+0.002}_{-0.002}$	$-0.061^{+0.002}_{-0.003}$
$\gamma_{1,CNO-p}$	-0.05 – 0.0	$-0.022^{+0.003}_{-0.003}$	$-0.022^{+0.004}_{-0.003}$
$\gamma_{0,He}$	1.5 – 2.0	$2.305^{+0.005}_{-0.004}$	$1.66^{+0.02}_{-0.02}$
$\gamma_{0,CNO}$	1.8 – 2.2	$2.348^{+0.005}_{-0.004}$	$1.91^{+0.02}_{-0.03}$
$R_{inj} \times 10^3$	3 – 15	–	$6.0^{+0.4}_{-0.3}$
s_{inj}	0.05 – 0.8	–	$0.35^{+0.03}_{-0.02}$
$D_0 [\text{cm}^2/\text{s}] \times 10^{28}$	2 – 6	$3.8^{+0.1}_{-0.2}$	$4.20^{+0.1}_{-0.09}$
δ_l	-1.2 – 0.0	$-1.14^{+0.06}_{-0.02}$	–
δ	0.2 – 1.0	$0.526^{+0.01}_{-0.008}$	$0.445^{+0.005}_{-0.005}$
$\delta_h - \delta$	-1.2 – 0.0	$-0.30^{+0.03}_{-0.03}$	$-0.22^{+0.02}_{-0.02}$
$R_{D,1} [\text{MeV}] \times 10^3$	1.5 – 8	$2.68^{+0.1}_{-0.07}$	–
$s_{D,1}$	0.05 – 0.6	$0.38^{+0.02}_{-0.02}$	–
$R_{D,2} [\text{MeV}] \times 10^5$	0.8 – 5	$3.5^{+0.6}_{-0.3}$	$4.0^{+0.6}_{-0.4}$
$s_{D,2}$	0.05 – 3.0	$0.61^{+0.1}_{-0.07}$	$0.39^{+0.09}_{-0.07}$
$v_{0,c} [\text{km/s}]$	0.0 – 30	1^{+2}_{-1}	–
$v_A [\text{km/s}]$	10.0 – 40	–	$18.4^{+0.9}_{-0.9}$
$\text{Abd}_C \times 10^3$	3.52 – 3.7	$3.670^{+0.008}_{-0.03}$	$3.71^{+0.03}_{-0.03}$
Abd_N	220 – 320	268^{+13}_{-20}	264^{+17}_{-15}
$\text{Abd}_O \times 10^3$	4.4 – 4.6	$4.47^{+0.03}_{-0.02}$	$4.38^{+0.03}_{-0.04}$
A_p	0.9 – 1.1	$1.021^{+0.002}_{-0.002}$	$1.026^{+0.002}_{-0.002}$
A_{He}	0.9 – 1.1	$1.023^{+0.004}_{-0.004}$	$1.006^{+0.004}_{-0.005}$
A_B	0.7 – 1.3	$1.08^{+0.01}_{-0.01}$	$1.10^{+0.01}_{-0.01}$
$A_{\bar{p}}$	0.7 – 1.3	$1.10^{+0.01}_{-0.01}$	$1.16^{+0.02}_{-0.02}$
$A_{xs^4He \rightarrow ^3He}$	0.7 – 1.3	$1.289^{+0.002}_{-0.01}$	$1.290^{+0.002}_{-0.01}$
$\delta_{xs^4He \rightarrow ^3He}$	-0.3 – 0.3	$0.05^{+0.02}_{-0.02}$	$0.25^{+0.01}_{-0.01}$
$A_{xs \rightarrow C}$	0.3 – 2.0	$0.66^{+0.07}_{-0.08}$	$0.38^{+0.08}_{-0.02}$
$\delta_{xs \rightarrow C}$	-0.3 – 0.3	$0.22^{+0.02}_{-0.08}$	$0.20^{+0.02}_{-0.1}$
$A_{xs \rightarrow N}$	0.7 – 1.3	$1.13^{+0.04}_{-0.03}$	$1.15^{+0.03}_{-0.05}$
$\delta_{xs \rightarrow N}$	-0.3 – 0.3	$-0.00^{+0.01}_{-0.02}$	$0.08^{+0.02}_{-0.02}$
$\delta_{xs \rightarrow B}$	-0.3 – 0.3	$0.02^{+0.01}_{-0.01}$	$0.13^{+0.01}_{-0.01}$

TABLE C.5 (cont.): Summary of the corresponding χ^2 values.

Parameter	# Datapoints	conv_HelMod	reacc_HelMod
χ_p^2	72	68.3	28.5
$\chi_{p,CALET}^2$	23	6.8	6.7
$\chi_{p,Voyager}^2$	6	9.8	37.4
χ_{He}^2	68	20.1	15.6
$\chi_{He,DAMPE}^2$	21	8.2	8.0
$\chi_{He,Voyager}^2$	7	99.7	14.0
$\chi_{\bar{p}/p}^2$	58	60.0	63.8
χ_C^2	68	26.8	26.7
χ_N^2	66	39.7	38.0
χ_O^2	67	8.9	11.8
$\chi_{B/C}^2$	67	25.9	27.7
$\chi_{B/C,DAMPE}^2$	13	17.4	11.3